



Increasing precipitation due to climate change could partially offset the impact of warming on glacier loss in the monsoon-influenced Himalaya until 2100 CE

Anya M. Schlich-Davies^{1,★}, Ann V. Rowan^{2,★}, Andrew N. Ross¹, Duncan J. Quincey³, and Vivi K. Pedersen⁴

¹Priestley International Centre for Climate, School of Earth and Environment, University of Leeds, Leeds, UK

²Department of Earth Science, University of Bergen and Bjerknes Centre for Climate Research, Bergen, Norway

³School of Geography, University of Leeds, Leeds, UK

⁴Department of Geoscience, Aarhus University, Aarhus C, Denmark

★These authors contributed equally to this work.

Correspondence: Ann V. Rowan (ann.rowan@uib.no)

Received: 14 March 2025 – Discussion started: 4 April 2025

Revised: 27 April 2026 – Accepted: 5 May 2026 – Published: 29 May 2026

Abstract. Glacier mass in the Himalaya is projected to shrink by 53 %–70 % due to climate change by 2100 CE. However, the impact of changes in precipitation amount and distribution on future glacier change remains uncertain because these variables are not often represented in glacier model projections. We explored the combined effects of past and future changes in air temperature and precipitation amount and distribution on the evolution of Khumbu Glacier in the Everest region of Nepal. We used a glacier modelling approach that forced an ice-dynamical glacier evolution model with surface mass balance calculations that included mesoscale meteorological variables derived from statistical downscaling of existing regional climate projections. Our simulations show that historical warming has committed Khumbu Glacier to mass loss of 10 %–23 % during this century, and that under an intermediate future emissions scenario (RCP4.5), this glacier could lose 70 % mass by 2100 CE due to warming. The projected increase in precipitation in tandem with warming could offset about half of the projected glacier loss, such that the total decrease in glacier mass by 2100 CE compared to the present day would be reduced to 34 %. However, under a higher future emissions scenario (RCP8.5) glacier loss due to warming will not be compensated by changes in precipitation, but will instead result in substantial ablation above 6000 m elevation, with devastating consequences for one of the highest glaciers on Earth.

1 Introduction

Projecting glacier change in response to climate change is important for determining the impact of anthropogenic warming on regional water availability (Pritchard, 2019). High Mountain Asia is projected to lose $34 \pm 19\%$ of glacier mass by 2100 CE if warming is limited to 1.5° to meet the ambitious Paris Agreement target (Kraaijenbrink et al., 2017). Less ambitious projections give $53 \pm 23\%$ glacier mass loss by 2100 CE under the intermediate emissions scenario RCP4.5, and $69 \pm 20\%$ under the high emissions scenario RCP8.5 (Kraaijenbrink et al., 2017; Marzeion et al., 2020; Rounce et al., 2023). Such projections are challenging to make, because accumulation and ablation processes in mountain environments are driven by orographic feedbacks between high-relief topography and atmospheric circulation systems such as the South Asian Summer Monsoon (e.g., Bookhagen and Burbank, 2006). Furthermore, large uncertainties arise from the challenge of simulating the interactions between the mass balance regimes of monsoon-influenced glaciers, where accumulation and ablation both occur during the monsoon season, and the dynamics of glaciers flowing through high-relief topography that includes processes such as the development of supraglacial debris layers that modify surface melting (Dehecq et al., 2019; Miles et al., 2018b; Salerno et al., 2023). Variability in the extent and intensity of the Indian Summer Monsoon during the Last

Glacial Maximum was shown to affect glacier expansion in the monsoon-influenced Himalaya through changes in snowfall distribution (Benn and Owen, 1998; Owen et al., 2009). Future Indian Summer Monsoon precipitation and variability projected in Global Circulation Models (GCMs) will increase with current global warming (Katzenberger et al., 2021), but as yet, the effect of projected changes in precipitation amount, timing, and phase (rain/snow) on Himalayan glaciers remain poorly constrained (Immerzeel et al., 2012; Mölg et al., 2014; Ragetli et al., 2016; Shaw et al., 2022; Shea et al., 2015).

Supraglacial debris covers 4%–7% of glacier surfaces globally and 30% of glacier ablation areas in the Himalaya, and modifies the response of glaciers to climate change relative to regional trends (Herreid and Pellicciotti, 2020; Kraaijenbrink et al., 2017; Rounce et al., 2023; Rowan et al., 2015). Satellite observations show that the rate of glacier mass loss across the Himalaya has accelerated over the last 40 years for both clean-ice glaciers and debris-covered glaciers (Maurer et al., 2019). Observations and modelling studies indicate that thick supraglacial debris caused historical mass loss from debris-covered glaciers to lag that of clean-ice glaciers, such that debris-covered glaciers are currently larger than would otherwise be the case (King et al., 2020; Rounce et al., 2023; Rowan et al., 2021). However, the dampening effect of supraglacial debris on glacier mass loss is overturned by the development of extensive supraglacial ponds and ice cliffs within debris layers (Miles et al., 2018a; Strickland et al., 2023) and the stagnation and detachment of debris-covered tongues from the upper and more active sections of these glaciers (Rowan et al., 2021). Quantifying the impact of feedbacks set up by the formation and expansion of supraglacial debris layers at a regional scale requires exploring such processes at scales that can be resolved in ice-dynamical glacier evolution models (Rowan et al., 2015; Nicholson et al., 2021; Compagno et al., 2022). These processes can be considered in 2-D (along the glacier flowline) either considering stochastic debris delivery to the glacier (Vacco et al., 2010) or continuous debris delivery, which can result in the over-accumulation of debris at the terminus (Anderson and Anderson, 2016; Ferguson and Vieli, 2021; Joutet et al., 2011), or in 3-D (using the horizontal and vertical ice-flow fields), which simulates the lateral transport and deposition of debris to the margins of the ablation area (Rowan et al., 2015; Wirbel et al., 2018). While recent rapid warming has resulted in a rise in regional equilibrium line altitude (ELA) and caused recession and collapse of glacier termini for both clean-ice glaciers and debris-covered glaciers (King et al., 2020), the decay of the former ablation areas of debris-covered glaciers is delayed by supraglacial debris, such that the terminus of the actively flowing glacier can remain in contact with the stagnant former ice tongue rather than separating (Maurer et al., 2019; Pellicciotti et al., 2015; Rowan et al., 2021).

In common with most large debris-covered Himalayan glaciers, Khumbu Glacier in the Everest region of Nepal (Fig. 1) is in greater imbalance with climate than a climatically equivalent clean-ice glacier, and has maintained a more extensive ice volume than would be possible without supraglacial debris (Rowan et al., 2021). Khumbu Glacier (RGI2000-v7.0-G-15-08331) is 16.0 km long with an area of 26.4 km². The median glacier elevation is 6025 m a.s.l. from the terminus at 4879 m a.s.l. to the headwall at 7981 m a.s.l. (RGI 7.0 Consortium, 2023). The stagnant debris-covered tongue has an area of 6.2 km² (23% of the total glacier). As a result of reduced ice flux from the accumulation area, the debris-covered tongue no longer receives much (or any) input of ice, and has dynamically detached from the active glacier (Fig. 1C); this observation is confirmed by the rapid reduction in ice flow and the peak in glacier surface lowering below the Khumbu Icefall where the debris layer is thinnest (King et al., 2020; Quincey et al., 2009). Observations and modelling of the dynamics and structure show that the tongue for 5 km upglacier from the terminus (25% of the total length, 20% of total ice volume) is stagnant and dynamically detached from the active glacier in the last century (Miles et al., 2022; Quincey et al., 2009; Rowan et al., 2021). Basal ice at the glacier surface indicates that the active terminus overrides the stagnant glacier tongue (Miles et al., 2021) and measurements of surface displacement show no longitudinal flow through the detached debris-covered tongue, which is collapsing laterally at a rate of about 3 m a⁻¹ (Watson et al., 2017). Therefore, the active glacier and the stagnant debris-covered tongue evolve along different trajectories, and only the part of Khumbu Glacier above the terminus of the active glacier can be considered dynamic (Miles et al., 2022). Projections of future glacier evolution should therefore discount the heavily debris-covered former tongue, which is decaying in situ without any input of new ice from the accumulation area, while considering the development of supraglacial debris across the ablation area of the active glacier.

We applied a novel glacier modelling approach to Khumbu Glacier to test the hypothesis that changes in precipitation in response to climate change will reduce the impact of warming on glacier mass loss. Khumbu Glacier is a benchmark debris-covered glacier in the monsoon-influenced Himalaya flowing from 7981 m above sea level (a.s.l.) to 4879 m a.s.l. that is representative in terms of elevation of the majority of glaciers in the Central and Eastern Himalaya (Fig. 1B). The “Little Ice Age” (LIA) maximum of Khumbu Glacier occurred about 200–500 years before present, which is consistent with ages produced for moraines elsewhere in the central Himalaya (Hornsey et al., 2022; Rowan, 2017). Khumbu Glacier was slightly larger than today during the late Holocene, transitioning from a clean-ice glacier with high velocities and efficient export of debris to a debris-covered glacier with lower velocities after the LIA; this change was initiated by the reduction in ice flux to the glacier

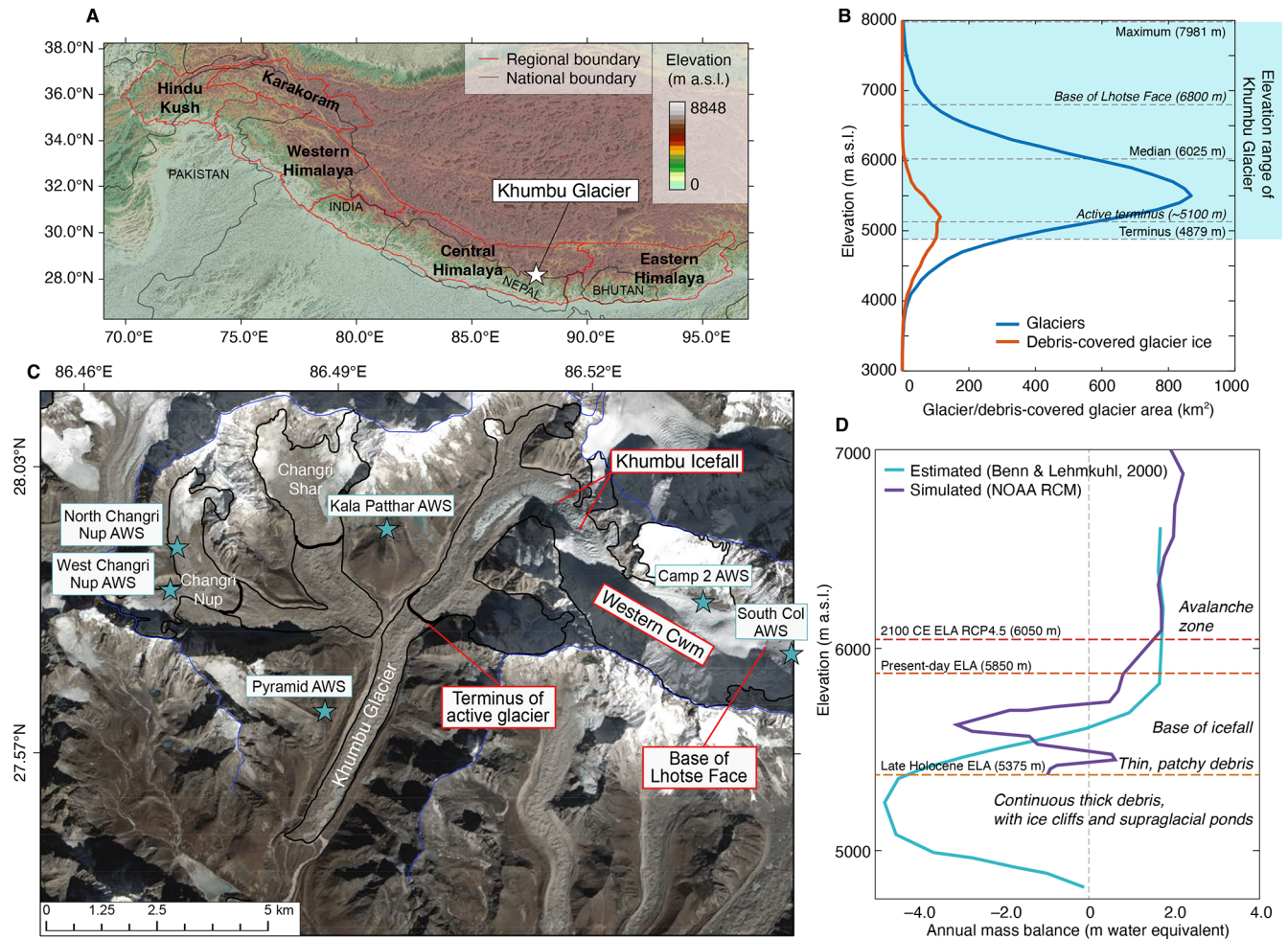


Figure 1. Khumbu Glacier location and context. (a) Map of High Mountain Asia showing the location of the monsoon-influenced Central and Eastern Himalaya and Khumbu Glacier. (b) hypsometry of glaciers and debris-covered glacier ice in the Central and Eastern Himalaya compared with the elevation range of Khumbu Glacier. (c) Map of Khumbu Glacier showing the glacier outline from the RGI database (black line) that is equivalent to the late Holocene (~ 1 ka) glacier extent identified from ice-marginal moraines, the hydrological catchment that represents the model domain (blue line), the extent of supraglacial debris, location of the Khumbu Icefall, the extent of active ice flow inferred from observations of glacier velocity, and location of the automatic weather stations (AWS) used for RCM downscaling (blue stars). (d) Estimated mass balance gradient for debris-covered glaciers in the Everest region (Benn and Lehmkuhl, 2000) compared with the glacier mass balance gradient simulated using the NOAA RCM, and showing change in the equilibrium line altitude (ELA) of Khumbu Glacier in the historical and future simulations for the NOAA RCM RCP4.5 experiment.

tongue promoted by a rise in ELA (Rowan et al., 2015). We used a 3-D ice-flow model forced by mass balance calculated from mesoscale meteorological variables to simulate the evolution of Khumbu Glacier from the late Holocene (~ 1 ka) through the present day (2015 CE) until 2100 CE using results from three downscaled Regional Climate Models (RCMs) under two Relative Concentration Pathways (RCPs). This approach represents an advance in the use of such models to understand the evolution of Himalayan glaciers whereby mesoscale meteorological forcing of surface mass balance is used with a thermomechanical glacier model to represent the processes of sublimation, snow avalanching, and debris transport, all of which are important controls on

the mass balance of Himalayan glaciers (Kneib et al., 2025). Simulations start from the late Holocene when Khumbu Glacier was last in dynamic equilibrium with the local climate, as evidenced by large ice-marginal moraines dated to 1.3 ± 0.1 ka surrounding the present-day glacier (Hornsey et al., 2022), and when the glacier surface was free of debris (Rowan et al., 2015).

2 Methods

2.1 Glacier model experimental design

The glacier model experiments used mesoscale meteorological variables to calculate surface mass balance for the Khumbu Glacier catchment in combination with a debris-covered glacier evolution model to represent the surface processes that modify mass balance (Fig. 2A). Our approach produced a total of six simulations of Khumbu Glacier to 2100 CE from the three Coordinated Regional Downscaling Experiment (CORDEX) South Asia region RCMs (NOAA, CCCma, IPSL; Lutz et al., 2016) under two RCPs (RCP4.5 and RCP8.5; Collins et al., 2013) to explore the impacts of possible variability in future precipitation amount and distribution in tandem with warming on glacier evolution. Before we used the RCMs to force the future climate scenarios, we evaluated their capabilities against observations of present-day weather and climate. The experimental design represents an advance compared with previous glacier modelling efforts by including in each simulation; (1) mesoscale meteorological phenomena, including sublimation, (2) the redistribution of surface mass by snow avalanching, and (3) the feedbacks between debris transport, ice flow and mass balance. This section describes the experimental design for the glacier modelling workflow, downscaling of the present-day RCMs using meteorological data from automatic weather stations (AWS) in the Khumbu Valley, downscaling of the future RCMs for both RCPs, the surface energy and mass balance calculations using COSIPY (Sauter et al., 2020) and the debris-covered glacier evolution modelling using iSOSIA (Rowan et al., 2015). A reference simulation and sensitivity experiments were carried out for the period 2013–2015 CE, and the simulations of future glacier change represented the period 2015–2100 CE. Additional information about the development and testing of the modelling approach is provided in Appendix A.

The spin-up simulation from the ice-free model domain to represent the late Holocene glacier was forced using a simple approximation of mass balance. The ice-free model domain was found by subtracting the estimated ice thickness (Farinotti et al., 2019) from a 30 m digital elevation model (DEM) acquired from the Shuttle Radar Topography Mission (Farr et al., 2007). The ice-free model domain incorporated the full hydrological catchment including the steep hillslopes in the Western Cwm that provide snow to the glacier surface by avalanching. As a starting point for our transient simulations of Khumbu Glacier, we reconstructed the late Holocene glacier from the ice-free domain using an ELA of 5325 m a.s.l. and an atmospheric lapse rate of $-4.0\text{ }^{\circ}\text{C km}^{-1}$ in a 5000 year simulation. Accumulation above the ELA was calculated as a function of elevation 0.2 mm m^{-1} up to a maximum of 2.0 m water equivalent (w.e.) per year and ablation was calculated as a function of elevation 0.5 mm m^{-1} up to a maximum of 2.0 m w.e. a^{-1} . This simulation con-

tinued through the LIA forced by a step change in mean annual air temperature (MAAT) equivalent to $1.5\text{ }^{\circ}\text{C}$ colder than the present day over 500 years following the approach of Rowan et al. (2015, 2021). Ice-marginal moraines denoting the late Holocene ($1.3 \pm 0.1\text{ ka}$) glacier extent and thickness (Hornsey et al., 2022) were used to constrain the spin-up simulation.

The late Holocene simulation was forced to present-day (2015 CE) conditions using three surface mass balances (one from each RCM) calculated using the Coupled Snowpack and Ice-surface Energy and Mass Balance model in Python (COSIPY v1.3) (Sauter et al., 2020). These simulations were evaluated against a range of observations of present-day glaciology and previous glacier model experiments (Fig. 3), and the experiment using the NOAA RCM was identified as the starting point for all future simulations because this was most representative of the observed glacier. We simulated only the active section of the glacier beyond 2015 CE and added the dynamically detached debris-covered tongue simulated at the present day to the model domain as a static topographic feature for the future simulations. The volume of the detached tongue was calculated by using the simulated present-day velocity field to separate the simulated present-day ice volume where velocities declined below 10 m a^{-1} . Thus, we arrived at the present-day from the LIA maximum simulation by forcing the LIA glacier with the 2015–2020 CE mass balance for 200 years.

We used the output from the present-day simulation with the 2095–2100 CE mass balance calculated using COSIPY to force the model to 2100 CE over a period of 85 years. The glacier model simulations continued from the present day to 2100 CE forced by distributed glacier surface mass balances calculated for each of the three RCMs and two RCPs using COSIPY. The three RCMs and two future RCPs represented a range of possible future climates with distinctly different precipitation trends – equivalent to dry, moderate, and wet scenarios for warming of $1.4\text{--}2.2\text{ }^{\circ}\text{C}$ under RCP4.5 and $3.8\text{--}4.1\text{ }^{\circ}$ under RCP8.5 (Table 1; Fig. 2D; Sect. 2.3). We used time slices representing the present day (2015–2020 CE) and the end of the 21st Century (2095–2100 CE) to calculate surface mass balance, and the preceding decade was used to evaluate these time slices (see Sect. 3.3). We used this step forcing, whereby the future mass balance was imposed and the glacier adjusted to this from the start of the century in question, rather than interpolating mass balance over time to reduce the computational expense of the surface mass balance and glacier modelling ($\sim 24\text{ h}$ per simulation).

Estimates from a global glacier modelling study indicate that avalanching contributes up to 18% of regional accumulation to glaciers in the monsoon-influenced Himalaya (Kneib et al., 2025) and observations of high-elevation Himalayan glaciers, including Khumbu Glacier, suggest that up to 75% of accumulation occurs by avalanching rather than direct snowfall (Fig. 1D) (Benn and Lehmkuhl, 2000; Laha et al., 2017). Avalanching affects mountain glaciers in two

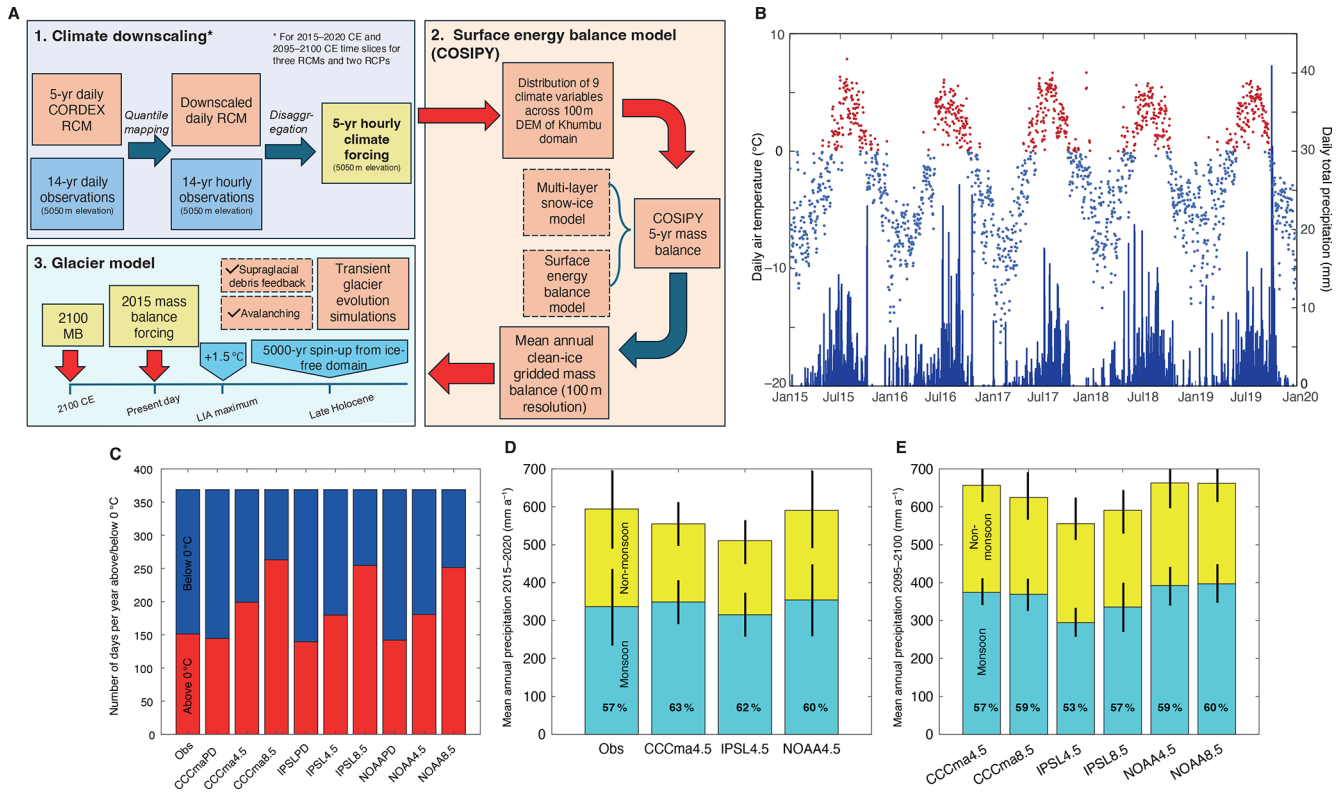


Figure 2. Glacier model experimental design and evaluation of RCM downscaling. **(a)** Schematic diagram of the glacier modelling approach showing the methods used for downscaling through quantile mapping and disaggregation of climate data. Surface energy balance modelling using COSIPY includes the preprocessing stage of meteorological distribution across the Khumbu domain, which is repeated for each RCM in the 2015–2020 CE climates and for the three RCMs and two RCPs for the 2095–2100 CE climates. The simulated mass balances are then used to force the iSOSIA model. **(b)** Daily mean temperature and daily total precipitation from the NOAA RCM for the present day (2015–2020 CE) following downscaling using quantile mapping with air temperature categorised into above freezing (red) and below freezing (blue). **(c)** Proportion of air temperatures above and below freezing for the present day for each RCM and RCP for the downscaled daily data compared with observations. **(d)** Annual precipitation totals for non-monsoon and monsoon with standard deviation between selected years shown by black bars for the downscaled daily data compared with observations. **(e)** Future (2095–2100 CE) time-slice annual precipitation totals for non-monsoon and monsoon months with standard deviation between selected years shown by black bars. In **(d)** and **(e)** the percentage of the total annual precipitation occurring during the monsoon is indicated by the value in bold text. (Obs = meteorological observations from AWS).

Table 1. Regional Climate Models (RCMs) chosen for this study and details of the Global Circulation Models (GCMs) from which these are derived.

CORDEX South Asia regional climate model	Driving CMIP5 global climate model	CMIP5 modelling centre	RCM name in this study	Future precipitation scenario (qualitative)	2100 CE mean temperature change from present day (°C)	
					RCP 4.5	RCP 8.5
ITTM-RegCM4	NOAA-GFDL-GFDL-ESM2M	National Oceanic and Atmospheric Administration (NOAA), USA	NOAA	Wet	1.4	3.8
IITM-RegCM4	CCCma-CanESM2	Canadian Centre for Climate Modelling and Analysis (CCCma), Canada	CCCma	Moderate	2.2	4.1
IITM-RegCM4	IPSL-CMSA-LR	Institut Pierre-Simon Laplace (IPSL), France	IPSL	Dry	1.6	3.8

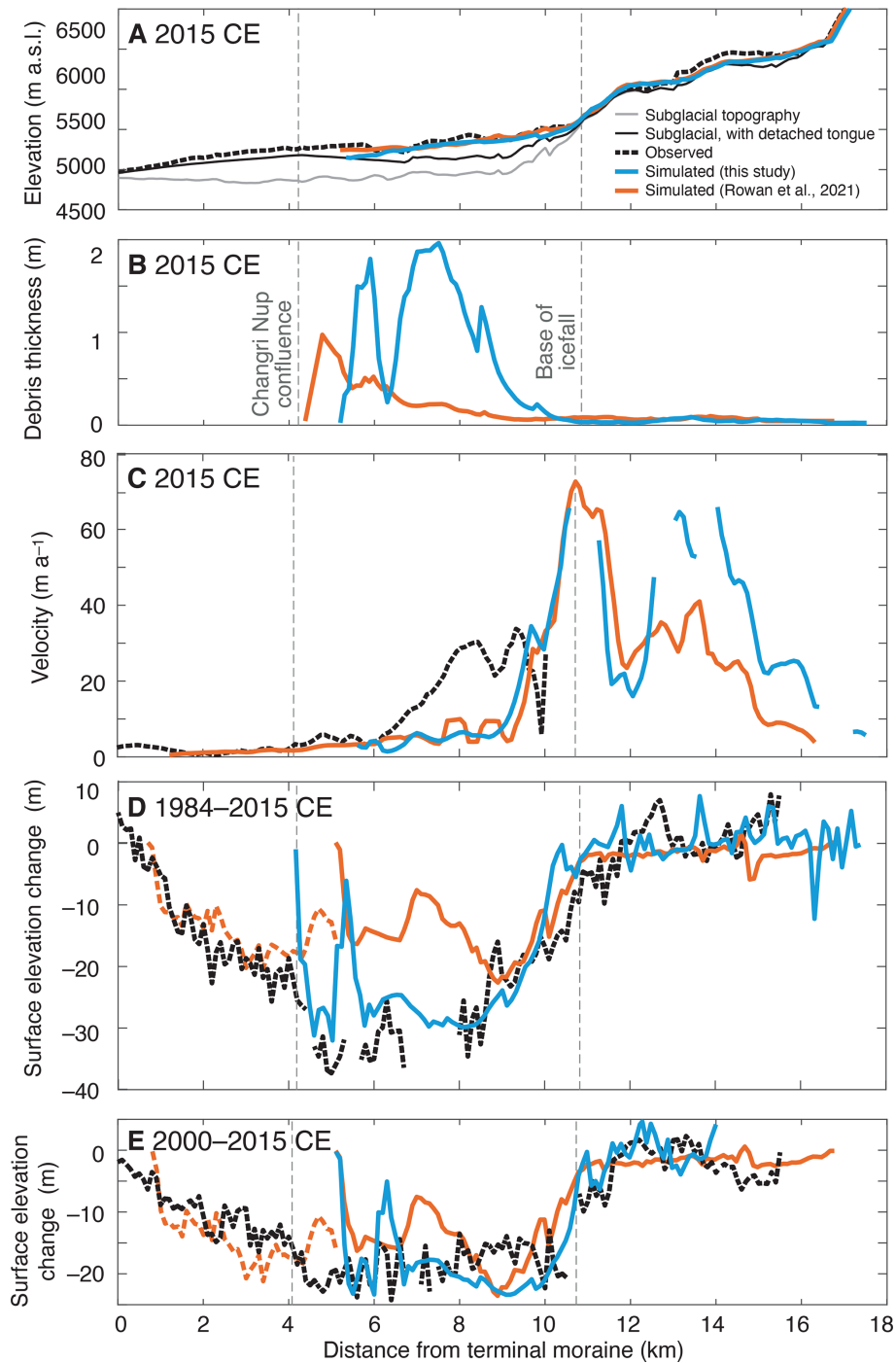


Figure 3. Evaluation of NOAA present-day simulation showing: (a) mean simulated glacier surface elevation and bed elevation calculated from a 500 m-wide swath profile along the central flowline of the glacier, and subglacial topography used in the entire glacier simulations in Rowan et al. (2015) was calculated by subtracting the ice thickness estimate (Farinotti et al., 2019) from the DEM, which represents an equivalent period. Subglacial topography including the dynamically detached debris-covered tongue added the simulated detached tongue to the initial subglacial topography, as described in Sect. 2.1. (b) mean simulated debris thickness, (c) simulated and observed velocities from the NASA MEaSUREs ITS_LIVE project (Dehecq et al., 2019), and simulated and observed mean surface elevation change between (d) 1984–2015 CE and (e) 2000–2015 CE using geodetic observations from King et al. (2020) compared with results from the simulations in this study and those in Rowan et al. (2021) where further information about the model evaluation can be found.

ways; (1) by moving snow from steep hillslopes onto the glacier surface thus increasing accumulation from that calculated from direct snowfall onto the glacier surface, and (2) by redistributing snow across steep sections of the glacier surface (Kneib et al., 2025). We examined the uncertainty in accumulation resulting from the application of a calculation in iSOSIA to move snowfall from slopes susceptible to avalanching (see Sect. 2.6). If avalanching was not considered in iSOSIA, then the accumulation of snow calculated using COSIPY within the catchment but outside of the glacier outline would have no impact on accumulation resulting in an underestimation of ice volume, and the steep sections of the glacier would hold more mass than expected. For example, when avalanching was not simulated and accumulation occurred at a uniform rate of $2.0 \text{ m w.e. a}^{-1}$ across the Western Cwm accumulation area, Khumbu Glacier had a similar extent but a volume more than double that of the glacier simulated with avalanche redistribution of snow, because mass was not redistributed effectively across steep sections of the glacier surface (result not shown).

2.2 Meteorological data collection and analysis

The first meteorological observations for the Nepal Himalaya were collected during the 1970s and found a trend of diurnal precipitation on ridges and nocturnal precipitation in valley floors (Ageta, 1976) reflecting cloud development from orographic convection during the day. Continuously recording AWS were first installed in the region in the 1990s at the Pyramid Observatory near Lobuche village, where Bollasina et al. (2002) analysed of the monsoon from meteorological observations collected between 1994 and 1999, finding that the onset (decay) of the Indian Summer Monsoon was distinguished by higher (lower) daily precipitation totals, mean relative humidity and atmospheric pressure and a reduced (increased) diurnal range in atmospheric temperature. Bollasina et al. (2002) identified two daily profiles in precipitation and wind direction thought to be related to the monsoon. In addition, five-day and ten-day precipitation cycles were observed linked to oscillations in the Tibetan High. A new AWS was installed at the Pyramid Observatory at 5035 m a.s.l. in September 2000 as part of a network in the Dudh Koshi valley of six AWS between 2680 to 5700 m a.s.l., in addition to some short-lived higher-elevation stations, maintained by the Ev-K2-CNR network. The Pyramid Observatory AWS included a snow depth sensor between 2009 and 2010, but the data were discontinuous and inconsistent, and the measurement period ended in December 2010. A second AWS was installed in the same location by the GlacioClim network in 2013 (Sherpa et al., 2017) provides a longer period of continuous data collection. More recently, a network of 5 AWS including the highest elevations in the Khumbu catchment were installed by the National Geographic project at Phortse (3810 m a.s.l.), Everest Base Camp (5315 m a.s.l.), Camp 2 (6464 m a.s.l.), the South Col (7945 m a.s.l.) and the Balcony

(8430 m a.s.l.) (Matthews et al., 2020). However, at time of writing, there are no continuous records of high-elevation meteorological variables that span a longer period than 15 years, making the calculation of climate normals impossible. In this study, we analysed data from these various sources for evaluation of mesoscale trends in the upper Khumbu Valley and for use to downscale RCMs and evaluate the results of our calculations. The location of the AWS is shown in Fig. 1C. Gaps in the air temperature and precipitation data were filled using interpolated data from neighbouring stations where required (as described in Appendix A).

The AWS data were used to make a reference simulation in COSIPY of the surface energy fluxes and mass balance of the Khumbu Glacier catchment between 2013–2015 for model development and sensitivity experiments (Figs. 4 and 5). We compiled 14 years of meteorological observations from the two AWS provided by the GlacioClim network at the Pyramid Observatory (5050 and 5035 m a.s.l.) and the West Changri Nup Glacier AWS (5363 m a.s.l.) (Sherpa et al., 2017). All meteorological data were collected for the period December 2010 to November 2019, apart from precipitation which was only recorded between December 2012 to November 2016. All meteorological data (excluding precipitation) used for the reference simulation were taken from the West Changri Nup AWS. Given the frequency of missing precipitation data from the AWS, the undercatch of snow associated with tipping bucket rain gauges, and the scarcity of high-elevation precipitation measurements, precipitation was not varied with elevation in the reference simulation. Precipitation data for the reference simulation were collected from the GlacioClim Geonor precipitation gauge at the Pyramid Observatory (5035 m a.s.l.) because this precipitation gauge provides a longer period of continuous observations than the other gauges and avoids errors due to low precipitation amounts measured by tipping bucket gauges, which are known to systematically underestimate snowfall particularly during high winds (Sherpa et al., 2017). Precipitation was measured at 15 min intervals using a Geonor T-200BM sensor mounted 1.8 m above the surface. Evaporation from the bucket was blocked by a layer of oil, but some loss did occur, as evidenced by precipitation values below 0 mm. Noise from wind and evaporation were corrected for by compensating any negative change over the 15 min time step with the neighbouring positive value such that accumulated precipitation was unchanged. Periods with prolonged evaporation were set to zero. Undercatch of snowfall by rainfall gauges was corrected through precipitation phase partitioning using wind speed observations (Wagnon et al., 2009). Air temperature was interpolated to match the height of the precipitation gauge using hourly lapse rates that averaged $-5.89 \text{ }^\circ\text{C km}^{-1}$. COSIPY was run for both elevations using the non-adjusted temperature data for 5336 m a.s.l. and the adjusted temperature data for 5035 m a.s.l. and it made little impact on the model results. Simulated meteorological variables were evaluated at the highest elevations

using the National Geographic AWS stations at Camp 2 (6464 m a.s.l.) and the South Col (7945 m a.s.l.) using data for May–November 2019 (Matthews et al., 2020).

Direct solar radiation across the model domain was corrected for the slope, azimuth, and shadowing potential of each pixel (Wohlfahrt et al., 2016; Sauter et al., 2020). A footprint-weighted correction was also applied to horizontal measurements of net radiation. The fraction of diffuse incoming shortwave radiation was estimated by using the ratio of total shortwave (global) radiation and potential shortwave radiation to define a clearness index (Wohlfahrt et al., 2016). This clearness index was used to calculate diffuse radiation, which was calibrated with data from the Neustift eddy covariance station in the Austrian Alps (Wohlfahrt et al., 2008). Pressure was distributed across the domain by first calculating sea-level pressure (cf. Lente and Ósz, 2020) and then interpolated with the barometric equation. The relative humidity gradient was calculated as $-0.002\% \text{ m}^{-1}$ using data from the Ev-K2-CNR and the GlacioClim AWS networks, and evaluated by comparison with measurements made by the National Geographic network AWS ranging in elevation from 3810–8430 m a.s.l. (Matthews et al., 2020) to capture trends at higher elevations. The distributed radiative fluxes were compared with the same high-elevation stations for 2019 to assess the efficacy of this method across the domain. Wind speed was assumed to be uniform across the domain.

2.3 Present-day RCM downscaling using meteorological observations

Six RCMs were assessed on their fidelity to present-day climate using hindcasting (Biemans et al., 2013) with an emphasis on temperature seasonality and seasonal precipitation dynamics given the importance of these variables for glacier mass balance. RCMs from the CORDEX South Asia domain were dynamically downscaled from CMIP5 GCMs by the Indian Institute of Tropical Meteorology to a 50 km spatial resolution (Lutz et al., 2016) and collected for the grid box containing Khumbu Glacier (27.9065056° N, 86.4352951° E). Three of the six CORDEX South Asia RCMs (NOAA, CC-Cma, IPSL) spanning a range of possible future precipitation conditions (Table 1) were selected as discrete scenarios for the glacier surface energy and mass balance calculations. The three remaining RCMs were discounted due to being intermediate to those selected for our experiments (i.e. close to the future precipitation scenario represented by CCCma) or particularly poor at reproducing seasonal temperature and precipitation cycles. For example, despite the annual precipitation sums from the CSIRO RCM being closest to observed values and having the potential to be the “driest” scenario examined, analysis of precipitation seasonality indicated that the monsoon signal was completely absent with this RCM instead showing a strong dominance of winter precipitation.

The present-day RCM results were downscaled using quantile mapping, also known as “distribution mapping”,

using 14 years of observations collected between January 2006 and November 2019 from three AWS as described in Sect. 2.2. Parametric quantile mapping (Piani et al., 2010) was used to downscale the RCM to a daily time step at the resolution of the DEM, whereby a statistical relationship between the raw climate model outputs and observations was formed by substituting the RCM results with observations at a cumulative density function of the prescribed distribution (e.g., a Gaussian distribution for temperature; Luo et al., 2018; a gamma distribution for precipitation; Piani et al., 2010). This correction was applied to the raw RCM outputs to produce a third downscaled dataset which had an improved fit to the observations (Fig. 2C and D). The quantile mapping approach was chosen because this is effective for downscaling precipitation and reduces errors in the standard deviation, the coefficient of variation, and the skewness of distributed values relative to other methods (Lafon et al., 2013; Reiter et al., 2018). The AWS data were used to disaggregate the daily downscaled present-day and end-of-century climate model outputs to an hourly resolution for energy balance modelling. All meteorological variables, excluding precipitation, were downscaled using the MELODIST Python tool (Förster et al., 2016). Seasonal means were applied for precipitation to reproduce the “nocturnal peak” seen during the monsoon that MELODIST was unable to replicate (Figs. A1, A2 and A3). Further information on the meteorological data analysis and RCM downscaling are provided in Appendix A.

2.4 Future RCM downscaling

Two future emission scenarios (RCP4.5 and RCP8.5) were available from CORDEX South Asia, which represent intermediate and high emissions by 2100 CE relative to the present day. These two emissions scenarios are frequently used in climate impact studies enabling the comparison of our results with studies that use other climate/glacier model projections. The two future emissions scenarios were analysed for each of the three CORDEX RCMs to account for the inherently high uncertainties in future precipitation trends associated with climate models and the interplay of changing precipitation with atmospheric warming. The same statistical downscaling approach and disaggregation used for the three present-day RCMs described in Sect. 2.3 was applied to the raw CORDEX RCM daily outputs for the three future RCM time slices under RCP4.5 and RCP8.5. The temperature change between the present day and the future time slices was preserved and there was no evidence of any imposed strengthening in the monsoon resulting from downscaling. An increase in the frequency of days per year outside of the monsoon season with high precipitation amounts (defined here as over 15 mm of daily precipitation) accounted in large part for the higher annual precipitation amounts relative to the present day that were found in four out of the six RCMs. However, the total future annual precipitation increase was on average 8.8% greater in the downscaled cli-

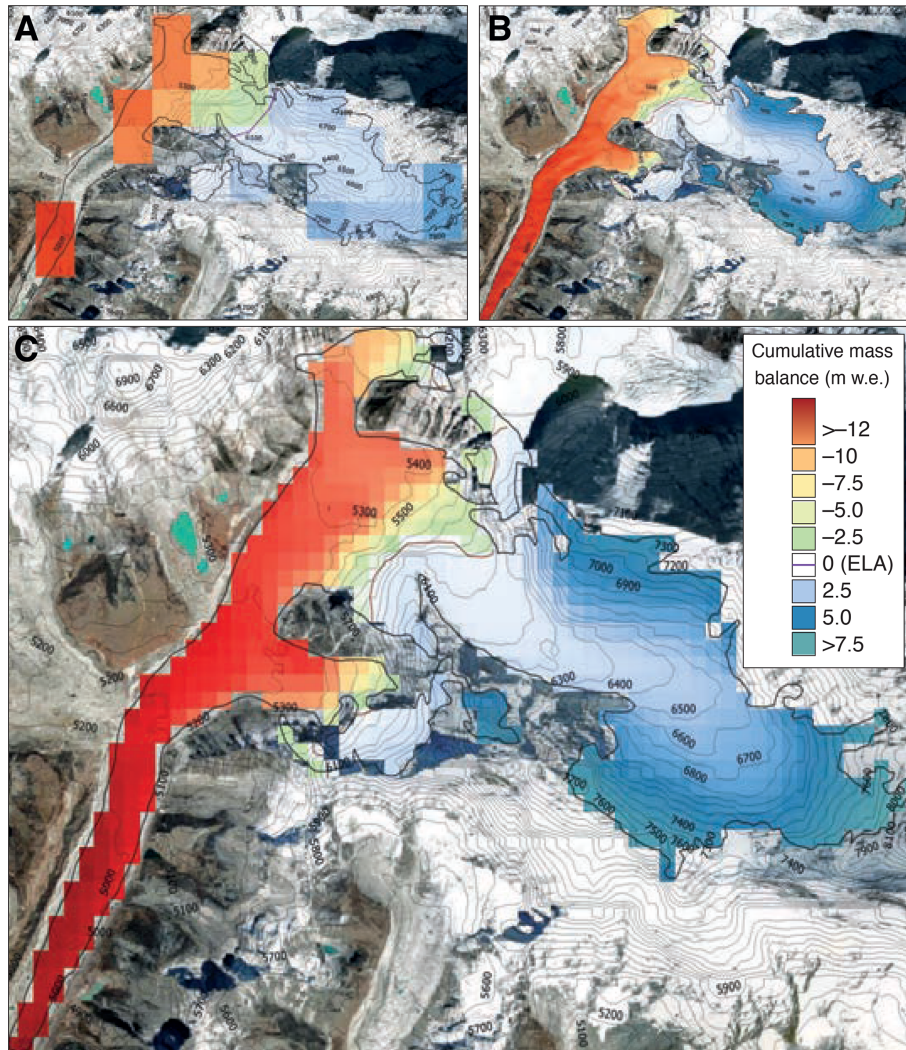


Figure 4. COSIPY reference calculation of present-day mass balance for Khumbu Glacier for the period 2013–2015 CE showing the results from calculations using different grid spacings using (a) a 1 km grid, (b) a 30 m grid, (c) the 200 m grid spacing used throughout the experiments in this study.

mates relative to the raw RCMs, suggesting that this positive trend was inflated by downscaling. The downscaled climates reduced the frequency of precipitation, although, as in present day observations, monsoon precipitation occurred frequently and could be characterised as predominantly drizzle in the future.

2.5 Surface energy balance modelling

COSIPY is a leading open-source method for estimating glacier surface mass balance and has previously been applied to glaciers in High Mountain Asia. COSIPY includes a calculation of sublimation, which is an important ablation process for high-elevation glaciers because ablation can still occur if the latent heat flux is negative through sublimation, even in instances where surface temperature and/or air tem-

perature are well below the melting point (Bonekamp et al., 2021; Brun et al., 2023; Huintjes et al., 2015). COSIPY resolves all energy fluxes (F) at the ice surface that contribute to surface melt (Q_{melt}):

$$F = SW_{\text{in}} \cdot (1 - \alpha) + LW_{\text{in}} + LW_{\text{out}} + Q_{\text{sens}} + Q_{\text{lat}} + Q_{\text{g}} + Q_{\text{liq}} \quad (1)$$

Where SW_{in} is incoming shortwave radiation, α is albedo, LW_{in} and LW_{out} are incoming and outgoing longwave radiation, and Q_{sens} , Q_{lat} , and Q_{g} are the sensible, latent, and ground heat fluxes (Oerlemans, 2001) and Q_{liq} is the heat flux from liquid precipitation; the latter variable is often neglected in ablation calculations (Cuffey and Paterson, 2010) but is of particular importance here as the Indian Summer Monsoon brings a significant amount of liquid precipitation to the lower reaches of Khumbu Glacier. The resulting F is

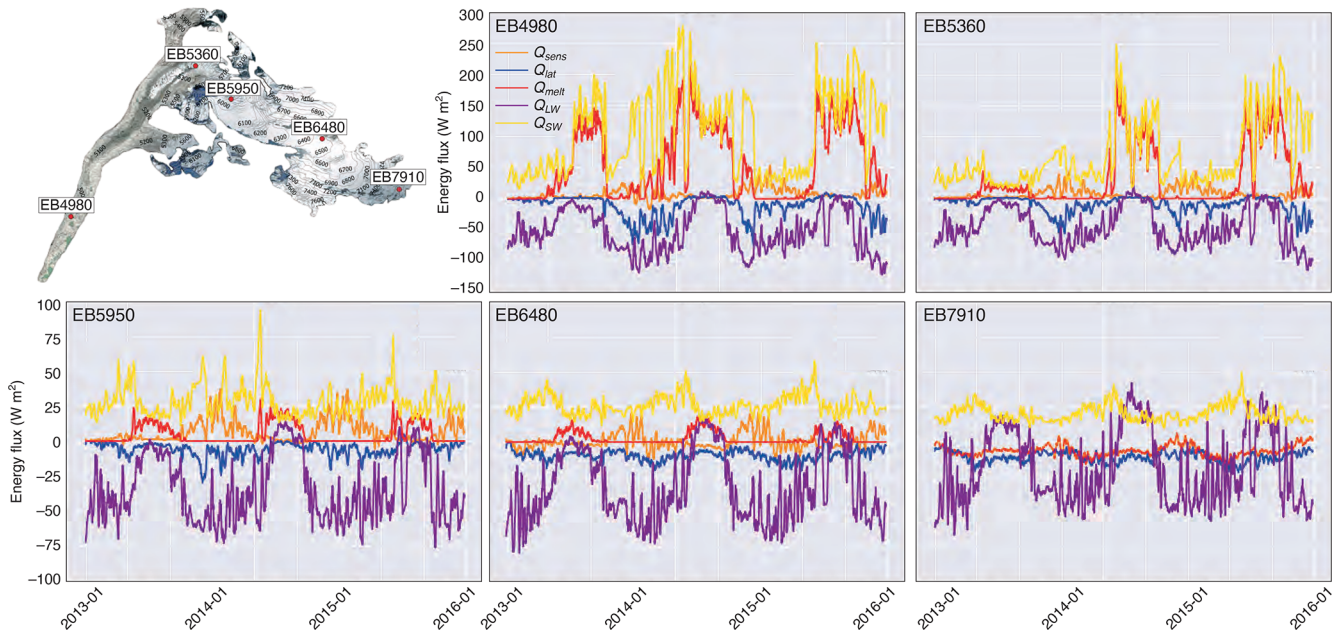


Figure 5. Locations of energy balance calculation points used for energy flux and melt components analysis in the reference calculation and sensitivity tests (named after their corresponding altitude e.g., EB6480) showing 5 d average of energy fluxes across study period for each site. Note that scales for energy flux are different for the two sites below the icefall compared to the three sites above the icefall.

equal to the energy available for surface melt (Q_{melt}) when surface temperature (T_s) is at melting point (0°C). T_s is used to calculate LW_{out} , Q_{sens} , Q_{lat} , Q_g and to partition solid and liquid precipitation. When T_s exceeds the melting point it is reset to 0°C (273.15 K) and the residual F fluxes equal Q_{melt} . In this instance, subsurface melt is triggered when the energy fluxes, for example, penetrating SW_{in} warm the ice layer so that T_s exceeds the melting point of ice (Sauter et al., 2020).

The COSIPY model domain was taken from the 30 m DEM that was resampled to 200 m grid spacing following a reference simulation for 2013–2015 and sensitivity analyses, which revealed minimal impact on the results whilst greatly reducing computational expense (Fig. 4). The sensitivity of glacier mass balance to individual meteorological variables (MAAT, radiative fluxes, relative humidity, lapse rate, precipitation amount, precipitation phase, glacier surface roughness) was calculated in sensitivity experiments using the reference simulation that perturbed these variables individually. Perturbations were made within the range of the possible uncertainties for each variable that arise from a combination of the choice of observations or climate models, the downscaling approach used, and the distribution of meteorological variables (see Sect. 3.1). The values used for perturbations of MAAT and precipitation amount were similar to those expected for possible future climate forcings. We tested a range of lapse rates from -3.0 to $-6.0^\circ\text{C km}^{-1}$ while maintaining the same ELA based on the range of monthly values calculated from regression of NASA MODIS land surface tem-

perature data for the Central Himalaya, which resulted in a difference in ice volume of $0.4 \times 10^9 \text{ m}^3$ and no change in glacier length at the present day (result not shown).

The downscaled and disaggregated CORDEX RCM daily climate variables (temperature, precipitation, the radiation components, wind speed, relative humidity and atmospheric pressure) were used to force COSIPY for the periods 2015–2020 and 2095–2100 CE. While snowfall measurements can be used as an input to COSIPY, there are no good-quality measurements of snowfall in the Everest region and so precipitation was partitioned into rainfall and snowfall using the snow transfer scheme within COSIPY (Sauter et al., 2020). COSIPY was forced using hourly meteorology with nine variables to calculate the energy balance and mass balance components at an hourly time step from the sum of accumulation by solid precipitation, deposition, and refreezing of melt water percolation, and ablation by melt and sublimation. The exchange processes at the surface, including energy release and consumption with phase changes, control temperature distribution and phase changes within the glacier (comprised of horizontal ice and snow layers), and accounts for meltwater refreeze and percolation with the meltwater produced from the surface melt calculations acting as an input. The impacts of supraglacial debris on ablation and of snow avalanching on accumulation were handled in iSOSIA, as described in the next section.

2.6 Ice-dynamical glacier evolution modelling

The second-order shallow ice approximation model (iSOSIA) is a 3-D higher-order ice-dynamical glacier evolution model that solves for the flow of ice including longitudinal and transverse stress gradients that are imposed on ice flow through high-relief topography (Egholm et al., 2011). This glacier model simulates the evolution of debris-covered glaciers by incorporating the feedbacks between debris transport, mass balance and ice flow (Rowan et al., 2015) and includes two processes that are important for many Himalayan glaciers; (1) the redistribution of snow by avalanching that is estimated to account for up to 75 % of accumulation, and (2) the formation and evolution of a supraglacial debris layer that insulates the ice surface to modify ablation (Rowan et al., 2015). While previous versions of this glacier model used depth-integrated ice flow, this version simulates ice flow through Khumbu Glacier in 3-D as the ice thickness is divided into 20 vertical layers to calculate englacial debris transport (Rowan et al., 2015). The glacier model has a variable time step that can adjust up to a maximum of 0.1 years to allow greater computational efficiency.

The distributed surface mass balances calculated using COSIPY using the downscaled RCMs for the periods 2015–2020 and 2095–2100 CE were used as inputs to the glacier model with no change in forcing applied between these two periods. The model domain topography was the same in iSOSIA as that used in COSIPY. Surface processes within the glacier model modified the distribution of accumulation and ablation but this was not updated into the surface topography used in COSIPY. Simulated accumulation was the result of the total snowfall in each cell and avalanching of snow imposed for the accumulated snowpack from hillslopes by removing snow and ice from hillslopes greater than 28° and redistributing this mass across less steep surfaces using a non-linear hillslope flux model (Roering et al., 1999). The avalanching routine was found to be sufficient to prevent snow and ice accumulation on slopes that are observed to be free of glacier ice such as the southwest face of Sagarmatha (Mt. Everest) while allowing accumulation on steep sections of the glacier (Rowan et al., 2015) resulting in accumulation rates at the glacier surface in line with the limited available observations for Himalayan glaciers of 2 m w.e. a⁻¹ (Benn and Lehmkühl, 2000).

Rock avalanching is responsible for much of the debris accumulation on the glacier surface but there is little information about the magnitude and frequency of these events, so headwall erosion was assumed to be uniform at 1 mm a⁻¹ (Rowan et al., 2021). Debris produced by headwall erosion was delivered to the glacier surface using a similar non-linear hillslope flux model to snow avalanching. The reduction in ablation beneath supraglacial debris from clean-ice values was represented as a reciprocal function that scaled clean-ice ablation (b_{clean}) to give sub-debris melt (b_{debris}) as a function

of debris thickness (h):

$$b_{\text{debris}} = b_{\text{clean}} \times \frac{h_0}{h + h_0} \quad (2)$$

where h_0 is a constant representing the characteristic debris thickness at which the reduction in ablation due to insulation by supraglacial debris is 50 % of the value for an equivalent clean-ice surface (Anderson and Anderson, 2016; Rowan et al., 2021). The observed heterogeneity of surface ablation required a parameterisation of sub-debris melt representing the effects of differential ablation, which was represented in Eq. (2) using a value for h_0 of 0.8 m (Bartlett et al., 2021; Rowan et al., 2021; Strickland et al., 2023). We note that Eq. (2) represents an empirical calculation of the impact of supraglacial debris on glacier surface melt that is calibrated to observations of sub-debris melt rates for glaciers in the Central Himalaya (Rowan et al., 2021) and as such, changes in surface energy balance processes including vapour fluxes within the debris-covered section of the glacier are not included.

3 Results

3.1 COSIPY parameter perturbations

The spatially averaged mass balance was most sensitive to changes in MAAT (perturbed by ±1.5, 2.0 and 3.0 °C), LW_{in} and SW_{in} (±10 % and 20 %). Perturbations of relative humidity (±10 % and ±20 %) had the least impact on mass balance. The use of a seasonal lapse rate of 5.38 °C km⁻¹ yielded a spatially averaged mass balance that was 5.6 % less than the reference calculation value, while a diurnal lapse rate gave a mass balance that was only 0.45 % lower because the reference lapse rate was close to the mean of the day/night lapse rates, whereas the environmental lapse rate (6.50 °C km⁻¹) gave a mass balance that was 1.24 % higher than the reference value. The relatively small difference in mass balance due to the choice of lapse rate is due to the extremely high elevation of Khumbu Glacier, which means that MAAT is below 0 °C in the accumulation area for much of the year and a higher lapse rate does not affect rain/snow partitioning. The largest difference in mass balance due to the choice of lapse rate occurred just below the ELA and resulted in a difference of ±24 % in spatially averaged mass balance for this section of the glacier. The National Geographic AWS on Mt. Everest provided an opportunity to examine lapse rates at the highest elevations. For the period April–November 2019, the observed lapse rate was 4.68 °C km⁻¹ between Phortse (3810 m a.s.l.) and Everest Base Camp (5315 m a.s.l.), and 5.36 °C km⁻¹ between Camp II and South Col, similar to the value used in this study. The lapse rate above 8000 m a.s.l. was about 1.2 °C km⁻¹ greater than that below 5600 m a.s.l. between the two highest AWS at the South Col (7945 m a.s.l.) and the Balcony (8430 m a.s.l.)

indicating that in the highest-elevation sections of the catchment, lapse rates may be best represented by values considered suitable for the free atmosphere.

Coupled parameter testing was carried out to perturb precipitation and MAAT simultaneously. The most significant change in spatially averaged mass balance followed a 3 °C increase in MAAT and 20 % decrease in precipitation amount. The change in ablation following an increase in temperature of 1.5 °C was compensated by accumulation resulting from 20 % higher precipitation. The impact on mass balance of two precipitation phase (rain/snow) partitioning schemes was investigated and compared with the default snow transfer function in COSIPY; (1) using threshold temperatures of 0.5, 2.0, and 3.5 °C, and (2) using a calculation that smoothly scaled rain/snow partitioning from 100 % solid precipitation at -1 °C to 0 % solid precipitation at 4 °C. The height of the 0 °C isotherm during months that experienced significant ablation (May–September) fluctuated around 5125–6250 m a.s.l., which correlated with the elevations that experienced the greatest mass balance change with lapse rate. While the lapse rate used to distribute MAAT did not have a significant impact on glacier-wide mass balance, the elevation of the 0 °C isotherm from the pre-monsoon until the end of the monsoon was sensitive to the air temperature distribution.

The glacier ice surface roughness (z_0) value was 1.7 mm (Table 2), which is a reasonable estimate for clean-ice glaciers (Mölg et al., 2012). The z_0 values reported in the literature vary widely, even for clean-ice glaciers, and do not consider debris-covered glacier surfaces, and so two substantially different z_0 values were tested as end-members of the likely range in z_0 values for Khumbu Glacier. Values for z_0 of 0.1 mm from Midtre Lovénbreen in Svalbard (Irvine-Fynn et al., 2014) and August-One Glacier in China (Guo et al., 2018), and a value of 6.9 mm for the clean-ice section of Haut Glacier D’Arolla (Brock et al., 2006) were all tested in the reference simulation. Adjusting z_0 had minimal impact on mass balance, although a higher (lower) z_0 did result in slightly increased (decreased) mass balance.

3.2 Evaluation of the COSIPY surface energy balance model results

The reference simulation represented the period 2013–2015 CE and was forced with AWS data using the model parameters in Table 2. Turbulent fluxes and energy balance components across Khumbu Glacier were explored across the 2013–2015 reference period to assess the performance of COSIPY and understand their relative spatial importance (Fig. 5). The glacier-wide clean-ice mass balance for the three-year reference period was -3.4 m w.e., which equates to -1.13 m w.e. a⁻¹. Maximum ablation was up to 16.2 m w.e. over three years (Fig. 4). High precipitation events were observed to offset some ablation if they occurred outside the core monsoon season (e.g., in October

2013 and May 2014) but did not influence monsoon season ablation when high air temperatures and strong incoming radiative fluxes rapidly remove snow cover and drive melting. Higher minimum temperatures in winter 2013–2014 CE relative to the other winters did not significantly influence accumulation rates, which remained similar to those in 2014–2015 CE. Low precipitation amounts during the 2015 monsoon (286 mm in 2015, compared to 330.8 mm in 2013, and 333.9 mm in 2014) resulted in lower accumulation in the upper reaches of the glacier. The precipitation gradient was calibrated to $1 \times 10^{-5} \% \text{ m}^{-1}$ to match observed accumulation rates. However, this gradient largely arises from avalanching (Benn and Lehmkühl, 2000) which is challenging to represent in COSIPY and was instead handled in the glacier model (Sect. 2.6).

The energy available for ablation peaked in the pre-monsoon and monsoon, bringing higher rates of sublimation and subsurface melt in April–June (Fig. 5). Simulated sublimation occurred at all elevations, with the highest cumulative loss near the South Col (EB7910) where sublimation dominated mass balance and only slightly slowed from December until May. Sublimation rates were increasingly tied to seasonality with distance down-glacier, with rates on the lower section of the tongue (EB4980) increasing from April until the start of the monsoon in July. Calculated subsurface melt was negligible at or above the ELA (5950 m a.s.l.) whereas at lower elevations sub-surface melt dominated mass balance with a stronger seasonal cycle related to surface temperature. The interannual variability in subsurface melt was linked to surface temperature, although low simulated subsurface melt rates in the first year of the reference simulation were largely due to persistence of the initial snow cover that shielded the subsurface from relatively warm air temperatures until the subsurface adapted to local conditions. Refreezing occurred across the entire glacier, with a staggered onset due to increased elevation, and the absolute values were low (Fig. 5). The higher latent heat flux during the monsoon resulted in higher deposition of snow to the glacier at the lower elevations, with negligible rates at higher elevation. Similar absolute values and patterns are seen for condensation.

Calculated incoming shortwave radiation matched well with AWS observations, indicating that the radiation model in COSIPY performed well across the extreme relief of the Khumbu Glacier catchment. Net shortwave radiation contributed the largest energy input to the glacier surface at lower elevations, correlating most strongly with the energy available for melt, with a mean correlation coefficient of 0.79. There was high temporal variability related to variable cloud cover exhibited in the hourly incoming shortwave radiation forcing and fluctuating albedo during the warmer months with the melting of the snowpack. The high incoming shortwave radiation the upper reaches of the glacier indicate that low net shortwave radiation is not due to topographic shading. Net shortwave radiation was correlated with albedo ($r = 0.86$), and the persistence of snow through-

Table 2. COSIPY model parameters, where α is albedo (of fresh snow, firn and ice), t^* decay time from snow to firn, d^* the constant for the effect of snow depth on albedo, and z_0 surface roughness length.

Parameter	Value	Unit	Source
$\alpha_{\text{freshsnow}}$	0.85	–	Mölg et al. (2012); Wagnon et al. (2009)
α_{firn}	0.6	–	Knap and Oerlemans (1996); Mölg et al. (2012)
α_{ice}	0.3	–	Mölg et al. (2012)
t^*	20	days	Mölg et al. (2012)
d^*	1.0	cm	Mölg et al. (2012)
$z_{0\text{snow}}$	0.24	mm	Gromke et al. (2011)
$z_{0\text{firn}}$	4.0	mm	Brock et al. (2006)
$z_{0\text{ice}}$	1.7	mm	Brock et al. (2006)
z_0 ageing length (linearly from $z_{0\text{snow}}$ to $z_{0\text{firn}}$)	60	days	Mölg et al. (2012)

out much of the year reduced the energy available for melt. Net longwave radiation also contributed to the energy available for melt as the pattern of both fluxes corresponded. Between 5900–7900 m a.s.l., net longwave radiation sometimes exceeded zero during the monsoon, most likely due to heavy cloud cover and increased temperatures relative to the glacier surface. The latent heat flux was almost zero at the lower elevation sites as the arrival of the monsoon resulted in higher relative humidity, and this pattern was similar, but dampened, at higher elevation. At the South Col (EB7910) the energy available for melt correlated most closely with the sensible heat flux (Fig. 5).

Grid spacings for the model domain of 30, 50, 200 m and 1 km were tested to ensure that the COSIPY calculations captured orographic effects without unnecessary computational expense (Fig. 4). The simulated maximum accumulation rate did not change significantly with grid spacing, giving accumulation rates of 2.1–3.9 m w.e. at 6500–7000 m a.s.l. in the reference simulation. The 1 km grid spacing contained only 27 glacier points, and gave a similar spatial mean mass balance to the finer-resolution calculations, but there were large gaps in mass balance calculated across the glacier that affected the height of the ELA and significantly reduced the calculated maximum accumulation value. The 30 and 50 m grid spacings captured greater spatial variability in mass balance relative to the 200 m resolution calculation, particularly at elevations between 5200–5400 m a.s.l. (Fig. 4). However, as the ELA, and the calculated maximum and minimum mass balances were not significantly different between these finer-resolution calculations, the 200 m grid spacing was used throughout to benefit from the much reduced computational expense.

3.3 Evaluation of the RCM downscaling

The downscaled climate variables from the three RCMs for the present-day time slices (2015–2020 CE) were evaluated against 14 years of observations from three AWS to assess the representation of means, seasonality, diurnal cycles, day-to-day variability, and interannual variability (Fig. 2C and D). All three downscaled RCMs showed good agreement between MAAT (-2.15 ± 0.05 °C) and observed air temperature from the Pyramid AWS (Figs. A1 and A2). The representation of the monsoon was greatly improved by the RCM downscaling; temperature seasonality was well resolved following quantile mapping and the monthly mean and minimum air temperatures were similar to observations across the present-day time slice (Fig. A1). The monsoon stabilised air temperatures and reduced the range between minimum and maximum temperatures in the downscaled RCMs, which was in better agreement with AWS observations, but was not present in the raw RCMs prior to downscaling. We note that the downscaled maximum air temperature was at times higher than observations amongst all RCMs during the post-monsoon and winter (Fig. A1) but the distribution of downscaled air temperatures was similar to observed values (Fig. A2). Gamma-distribution quantile mapping substantially improved the absolute precipitation values relative to the AWS observations compared to those in the raw RCMs; the overestimation of winter precipitation and relative underestimation of monsoon precipitation amounts in the raw RCMs was reduced and downscaled results show a clearer monsoon signal (Fig. A3). When compared with AWS observations, RCM downscaling slightly overcorrected the seasonal precipitation pattern with a slight underestimation of winter precipitation for the most extreme winter

events. Across the three present-day RCM simulations, the surface mass balance calculated using the NOAA RCM was more positive than that for the ISPL and CCCma RCMs and most similar to the mass balance calculated from meteorological observations, and remained the most positive mass balance in the end-of-century time slices (Fig. 6).

3.4 Evaluation of the iSOSIA glacier evolution model results

COSIPY was used to calculate clean-ice surface mass balance from the downscaled RCMs, and the insulating effects of supraglacial debris were calculated in iSOSIA. The simulated glacier geometry and dynamics were compared with remotely sensed observations of ice thickness, supraglacial debris distribution, velocity, and surface elevation change for the present-day glacier (Fig. 3) and varied depending on the RCM used as forcing (Fig. 7). The experiment using the NOAA RCM was identified as the starting point for all future simulations because this was most representative of the observed glacier at 2015 CE (Fig. 3). The distributed surface mass balances calculated using COSIPY were most similar to observed values after the calculated surface mass balances were integrated with the glacier model to include accumulation by snow avalanching and the reduction in surface melting beneath supraglacial debris; the active glacier extent was underestimated if supraglacial debris is not simulated (Fig. 8). The supraglacial debris-mass balance feedback in the glacier model reproduced the observed reversed mass balance gradient and peak in ablation below the Khumbu Icefall (Fig. 1D).

The simulated glacier area was 7.8 km² and similar to that obtained from structural mapping in 1979 CE (Nakawo, 1986). Radio-echo sounding in 1999 CE obtained ice thickness estimates close to the active terminus of ~160 m (Gades et al., 2000) and simulated ice thickness at the terminus was 130 m (Fig. 3A). The simulated thickness at the active glacier terminus thickness was approximately 175 m in 1999 CE, which agreed well with observations from DEMs of difference that show thinning here of up to 55 m between 1984–2018 CE (Fig. 3D and E) (King et al., 2020). Simulated surface elevation change in the ablation area was –30 m over 20 years to the present day and similar to values derived from satellite observations for 1984–2018 CE (King et al., 2020). Simulated present-day glacier velocities (Fig. 9) reached a maximum of 248 m a⁻¹ and showed a similar pattern and magnitude to glacier surface velocities observed using remote sensing observations, which reach a maximum of 220 m a⁻¹ in the Khumbu Icefall (Altena and Kääb, 2020) and up to 20 m a⁻¹ in the ablation area (Quincey et al., 2009; Dehecq et al., 2019). The simulated present-day velocities in this study were a better fit to remote sensing observations than those from previous simulations that used an elevation-dependent mass balance forcing (Rowan et al., 2015, 2021) where the maximum simulated velocities were 118 m a⁻¹.

3.5 Climate change and glacier evolution from the present day until 2100 CE

Khumbu Glacier is responding to historical climate change and will continue to shrink even if warming ceases today. Indeed, if we allow the spin-up experiment to reach equilibrium with the present-day NOAA RCM mass balance, the glacier terminus will recede by 2.1 km and the maximum ice thickness will decrease from 246 to 206 m by 2100 CE without any additional warming. In this scenario, a supraglacial debris layer up to 1.3 m thick extends 1 km up-glacier from the terminus and partially dampens the committed volume loss, by sustaining 13 % more ice volume than would be the possible for a clean-ice glacier surface with the same mass balance (Fig. 10A). The committed glacier volume loss due to historical warming in the absence of any further climate forcing is 10 %–23 % of the present-day glacier mass (Fig. 10C) with the associated uncertainty represented by this range of values arising from the parameterisation of the impact of supraglacial debris evolution on surface melting.

Now considering the effects of additional warming under the RCP scenarios for the NOAA experiment, we find that greater warming occurs in winter than in the monsoon under both RCPs and results in an increase in annual precipitation amount of about 15 % made up of a greater increase in non-monsoon precipitation than monsoon precipitation (Fig. 2E). The climate forcing from the downscaled NOAA RCM under RCP4.5 is 1.4 °C warmer than the present day (–0.75 °C in 2095–2100 CE compared with –2.15 °C in 2015–2020 CE) and annual precipitation increases by 14.8 % from 581.4 mm at present day to 664.8 mm a⁻¹ by 2100 CE with monsoon (June–September) precipitation increasing by 5.4 % and non-monsoon season (December–February) precipitation increasing by 14.1 % (Fig. 2E). Under RCP8.5, the downscaled climate forcing is projected to be 3.8 °C warmer than present day (1.65 °C in 2095–2100 CE) with an increase in annual precipitation of 14.9 % by 2100 CE, with monsoon precipitation increasing by 9.8 % and non-monsoon precipitation increasing by 19.4 % (Fig. 2E).

In the NOAA RCM RCP4.5 experiment, the spatially averaged cumulative glacier mass balance is –0.14 m w.e. a⁻¹ in 2100 CE, which is slightly more positive than the present-day value of –0.21 m w.e. a⁻¹ (Fig. 6) and glacier volume decreases by 36 % between the present day and 2100 CE (Fig. 10C). While significant, this end-of-century glacier loss is partially offset by the concurrent increase in precipitation. In comparison, an equivalent simulation forced only by warming and without any change in precipitation results in a more linear trajectory of glacier change and 70 % loss of glacier volume by 2100 CE (cyan line in Fig. 10C) demonstrating that 34 % of potential glacier loss from warming could be compensated by the increase in precipitation that occurs as a result of warming.

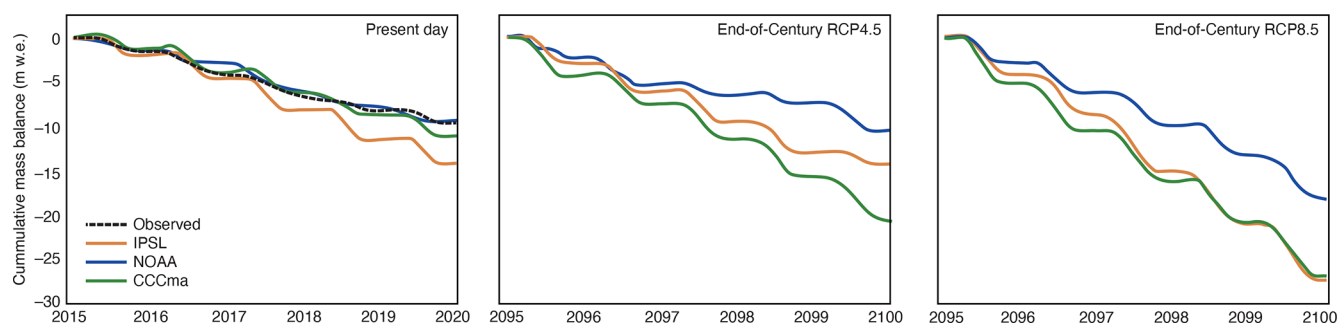


Figure 6. Spatially averaged cumulative clean-ice mass balance with clear seasonality for the present day time slice including the mass balance forced by the observations used for downscaling, and the end-of-Century time slice under RCP4.5 and RCP8.5. The low annual glacier-wide mass balance values shown here result from the extent of the model domain used to force the glacier model that includes the larger catchment beyond the glacier margins and therefore contains a higher proportion of lower elevations than those of the glacier itself. However the similarity between the mass balance results for simulations forced by NOAA RCM and observations can be clearly seen, and the differences between the three RCMs is apparent in all time slices.

3.6 Comparison of projections for different RCM forcings

The CCCma and IPSL RCMs projected greater warming from the present day by 2100 CE than the NOAA RCM under RCP4.5 with a value of 1.6°C ($+0.2^{\circ}\text{C}$ compared with the NOAA RCM) in the IPSL RCM experiment and 2.2°C ($+0.8^{\circ}\text{C}$) in the CCCma RCM experiment. These two RCMs also projected slightly greater warming by 2100 CE under RCP8.5, with a value of 3.9°C ($+0.1^{\circ}\text{C}$ compared with the NOAA RCM) for the IPSL RCM experiment and 4.1°C ($+0.3^{\circ}\text{C}$) for the CCCma RCM experiment.

The projected increase in precipitation amount across the three RCMs is similar between RCPs with annual totals above 600 mm by 2100 CE. The CCCma RCM gives the greatest increase in annual precipitation amount of 100 mm by 2100 CE (Fig. 2E). There is no evidence of change in the intensity of the Indian Summer Monsoon, as the seasonal split in precipitation remains similar to the present day, but the frequency of days with high precipitation (over 15 mm d^{-1}) increases by 2100 CE, giving twice as many days in the NOAA RCM experiment and up to seven times as many days in the IPSL RCM experiment.

Under RCP8.5, all experiments showed similar results for mass balance by 2100 CE with only a 10 % difference in glacier volume between the three RCMs (Fig. 10C). The CCCma RCM experiment has only a 1 % difference in volume loss between RCP4.5 and RCP8.5 by 2100 CE despite a 1.9°C difference in MAAT – this is a surprising result given the significant temperature difference, which can be attributed to the greater number of high-magnitude precipitation events that occur under RCP8.5 in combination with the small difference in winter temperatures between the two RCPs. Indeed, in the CCCma RCM experiment under RCP4.5, the maximum winter temperature is 1.7°C higher than for the other RCMs, resulting in ablation and rainfall (rather than snowfall) during the winter.

4 Discussion

4.1 Uncertainties associated with the glacier modelling

Sources of uncertainty in our results arose from each step of our glacier modelling workflow, and we considered how the experiments could be designed to reduce these uncertainties. Here we discuss the potential sources of uncertainty associated with the choice of RCMs, the downscaling of the RCMs, the use of time slices rather than continuous mass balance calculations, the representation of future precipitation in the RCMs, and the representation of avalanching in the glacier model.

A single RCM was not considered sufficient to represent both present-day climate and potential future climatic extremes, but the climate-mass balance forcing ensemble was limited in size due to the small number of RCMs available. The use of three RCMs allowed the implications of uncertainties in understanding of local climate for glacier evolution to be evaluated. A multi-model mean approach using all the CORDEX South Asia RCMs (as widely used elsewhere) was not considered sufficient to represent present-day and future climate conditions in the Khumbu Valley because this approach gives equal weighting to models irrespective of their performance (Pierce et al., 2009) and does not enable intercomparison of results for future climate conditions.

Five-year downscaled RCM time slices were chosen to reduce computational expense associated with COSIPY and the integration with iSOSIA. To ensure that the five-year periods selected were representative, the preceding decade was used for comparison with the time-slice results (results not shown). The use of quantile mapping with 14 years of AWS data as the downscaling method limited the influence of any natural variability by ensuring that the period did not reflect an extreme phase of natural climate oscillation. This comparison was particularly important for the future time slices, where large uncertainties arise between RCMs, and obser-

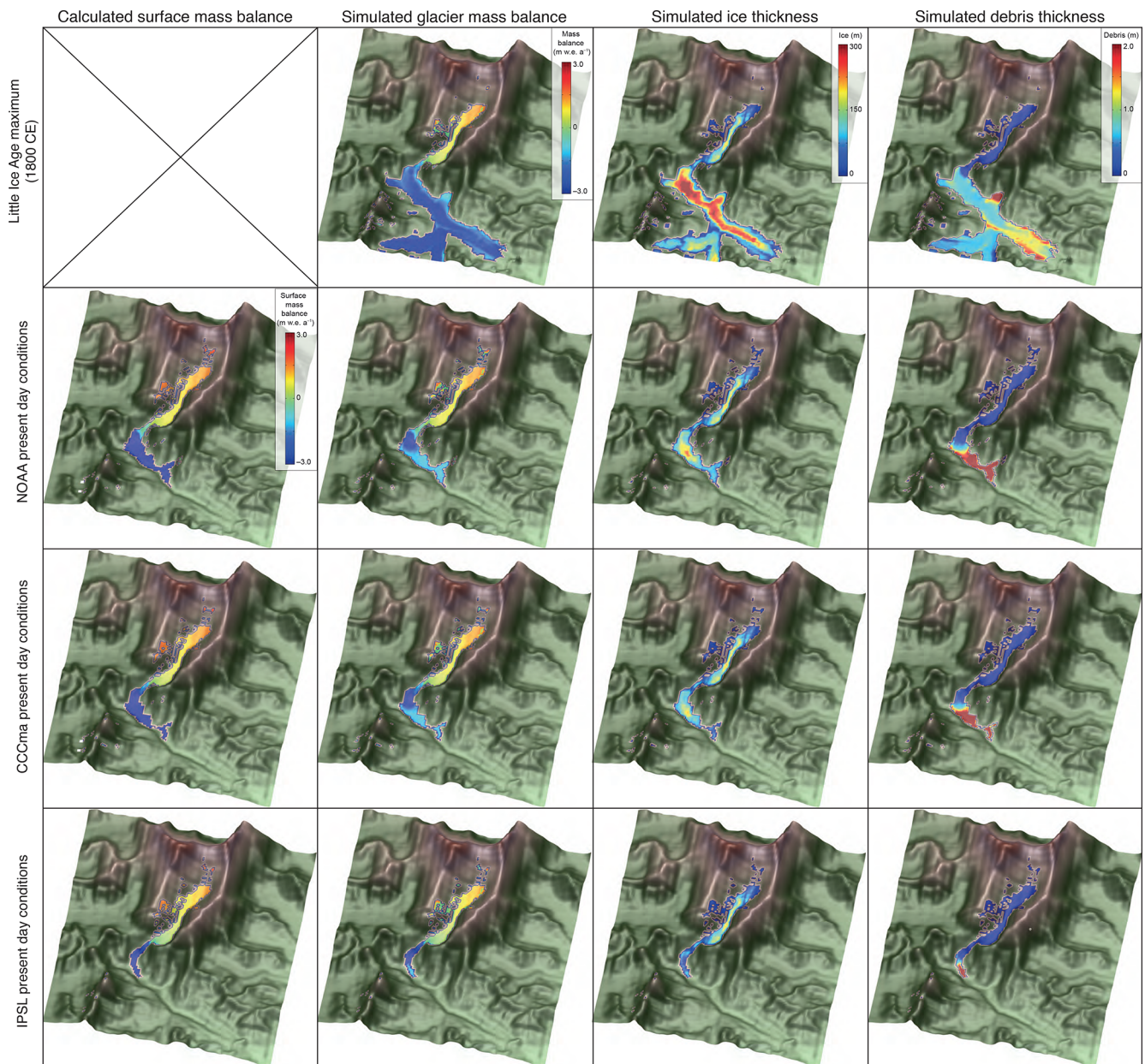


Figure 7. iSOSIA model sensitivity to surface energy and mass balance forcing, showing “Little Ice Age” (~1800 CE) maximum glacier mass balance, ice thickness and debris thickness. Present-day results for surface mass balance calculated using each RCM with COSIPY showing glacier mass balance calculated using the same climate forcing following integration with the glacier model, simulated ice thickness, and simulated debris thickness.

vational data cannot be used for evaluation of the down-scaled climate or the resulting mass balance. We note that this experimental design could be improved by interpolating the mass balance over time and coupling the COSIPY and iSOSIA models such that mass balance was calculated dynamically for the evolving ice surface, but this was beyond the scope of our experiments. However, the experiments were repeated using additional mid-Century (2045–2050 CE) mass balance forcings to investigate if this produced a differ-

ent end-of-Century result. These experiments produced near-identical results in 2100 CE to the experiments with no mid-Century forcing, in part because the response time of the simulated glaciers was longer than the 40-year period between the present-day and future time slices. Thus, a mid-century surface mass balance forcing was not considered necessary in our experiments and instead we used a step forcing for mass balance rather than interpolation between mass balance calculations in the glacier model.

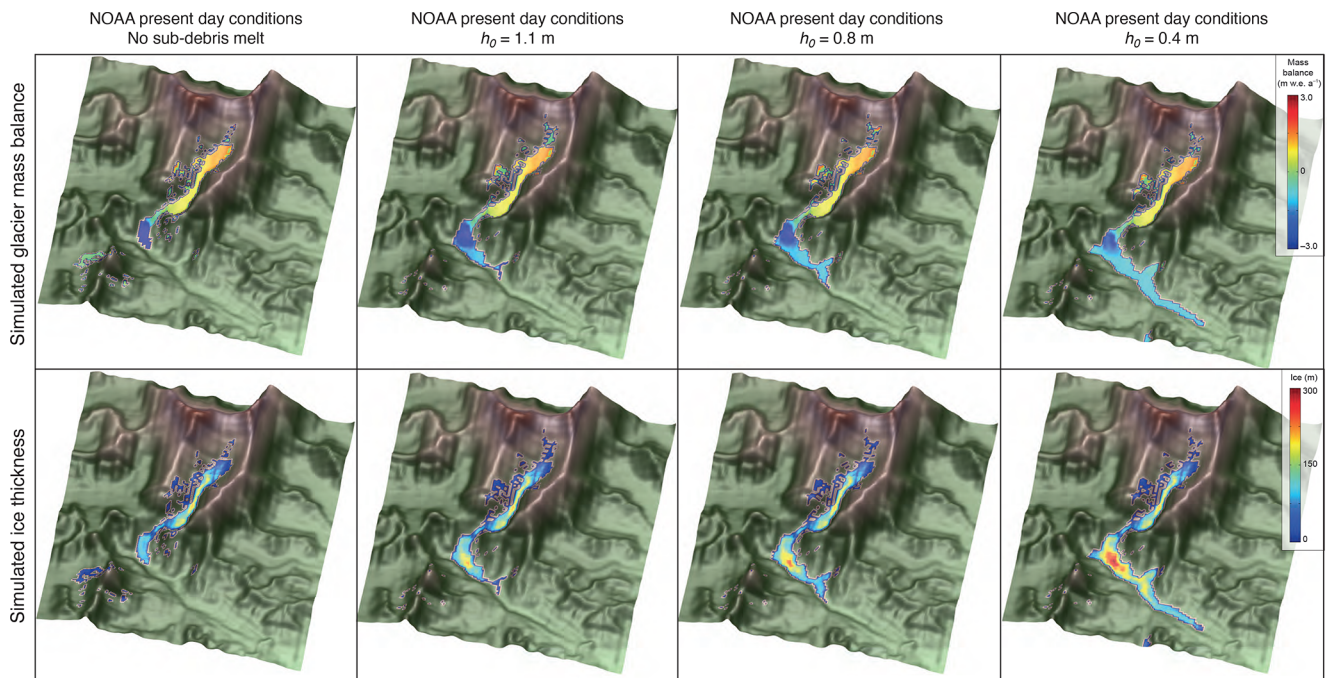


Figure 8. Glacier mass balance and ice thickness simulated using the NOAA RCM climate forcing and the resulting simulated ice thickness where no sub-debris melt is imposed and the glacier has an entirely debris-free surface compared with ice results for simulations with h_0 values of 0.4, 0.8, and 1.1 m where h_0 is a constant in Equation (1) representing the characteristic debris thickness at which the reduction in ablation due to insulation by supraglacial debris is 50 % of the value for an equivalent clean-ice surface (Anderson and Anderson, 2016; Rowan et al., 2021).

The differences in simulated glacier change and response time between RCM forcings were at times greater than those resulting from the RCP due to differences in projections of precipitation. Whilst the three selected RCMs performed well in representing annual precipitation cycles from the six available CORDEX RCMs, we note that this representation was still fairly poor, although substantially improved by quantile mapping (Fig. 2D). The poor representation of monsoon dynamics in the present-day RCMs highlights an additional uncertainty associated with future precipitation scenarios and that these results should be treated as a set of possible scenarios.

The CORDEX CMIP5 and CMIP6 projects only produced dynamically downscaled RCMs for two future emissions scenarios (RCP4.5 and RCP8.5) and as such the implications of other RCPs for glacier evolution could not be assessed. The downscaled future climates were compared with those from other studies using CORDEX results, and showed similar annual and seasonal regional temperature trends strongly linked to the choice of RCP, and similar positive precipitation trends with poor agreement between RCMs (Kaini et al., 2019; Sanjay et al., 2017). The relationship between precipitation and warming in the two future emissions scenarios was less clear than that for air temperatures because the monsoon-influenced Himalaya has particularly poor RCM consensus and high levels of uncertainty in future precipi-

tation trends with warming relative to other regions in High Mountain Asia (Sanjay et al., 2017).

A potentially large uncertainty in the glacier model arose from the parameterisation of avalanching, as this mass balance variable is poorly constrained, with no direct observations of the avalanche contribution to the mass balance of Khumbu Glacier and high regional variability (Kneib et al., 2025). Avalanching was included in iSOSIA by slope-dependent diffusion and resulted in increased accumulation along the glacier surface in the Western Cwm and improved the agreement between simulated and estimated accumulation rates and distribution (Fig. 1D). Future work to resolve the impact of low frequency–high magnitude avalanche events on accumulation rates would be useful to refine this calculation but the contribution of avalanches to glacier accumulation over decadal time scales remains extremely challenging to measure (Purdie et al., 2025).

4.2 Impacts of mesoscale and microscale meteorology on glacier change

Our study addresses fine-scale temporal (hourly) and spatial (100 m) glacier surface processes, including avalanching and sublimation, that affect glacier surface mass balance across the elevation range of Khumbu Glacier, but further observations of meteorological and glaciological conditions at the

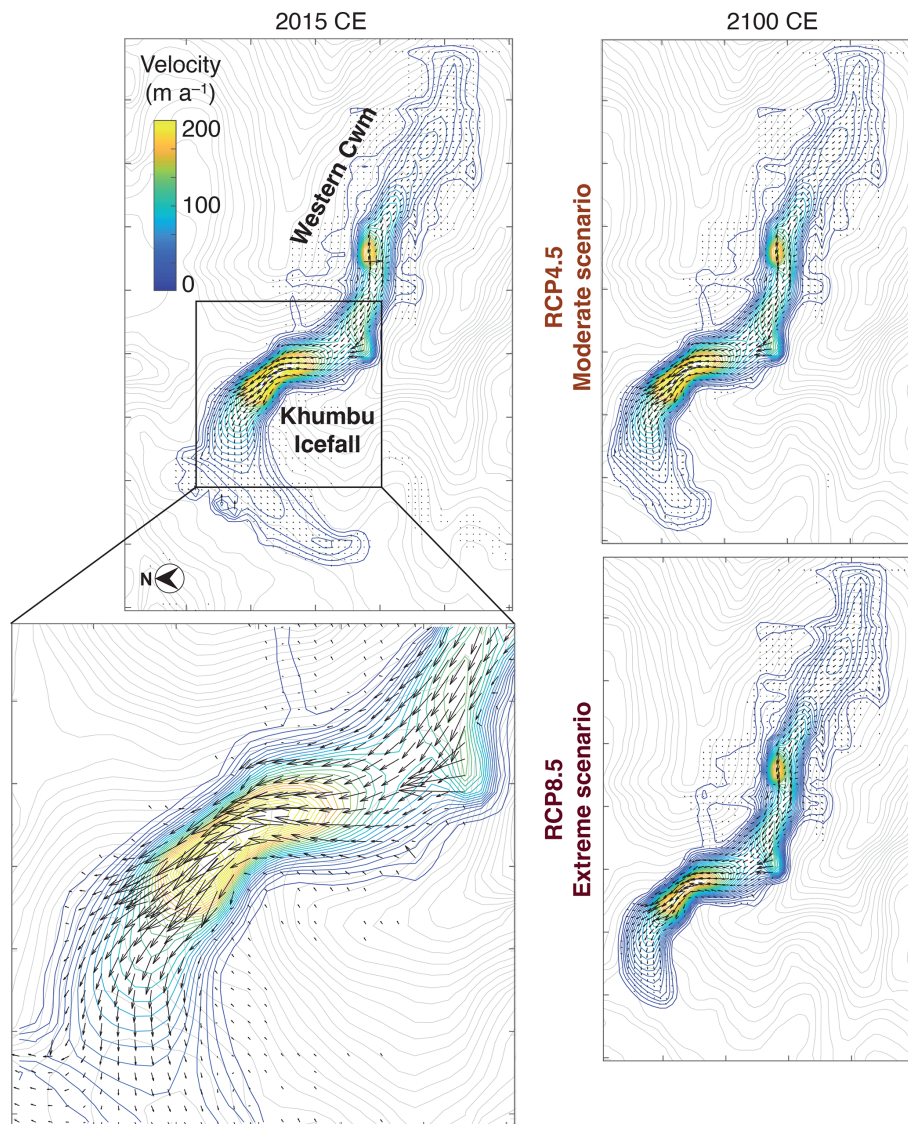


Figure 9. Simulated ice flow for Khumbu Glacier. Velocity-vector maps showing simulated ice flow magnitude and direction from the present day (2015–2020 CE) and 2100 CE under RCP4.5 and RCP8.5 using the downscaled NOAA climate forcing. Simulated ice flow speed is shown as colour shading with blue contours, and the bed topography is shown by grey contours. The outermost contour in each plot represents the slowest ice flow close to the glacier margins with depth-integrated velocities of $5\text{--}10\text{ m a}^{-1}$. Note that rapid flow across the Western Cwm indicated by a single arrow represents the effects of avalanching rather than sustained glacier flow.

highest elevations would be beneficial, and are needed if micro-scale processes are to be included in glacier models (Brun et al., 2023; Khadka et al., 2021; Mölg et al., 2014; Shaw et al., 2022). Analysis of meteorological observations from AWS across the Dudh Koshi catchment indicated that precipitation gradients were weak, slightly negative or absent, confirming the observations of Salerno et al. (2015) and Yang et al. (2017). To test the sensitivity of precipitation to elevation, COSIPY was forced by a gridded climate distributed using weak negative, weak positive, and no precipitation gradients distributed across the model domain using a linear regression with elevation from the 100 m resolution

DEM. The results of these experiments were used to force iSOSIA and the simulated historical glacier evolution was similar, resulting in only a 10 m difference in the maximum ice thickness between simulations with different precipitation gradients (result not shown).

The mass balance sensitivity to seasonal and daily variations in lapse rate showed a lesser impact on glacier-wide mass balance than in other studies, due to the large elevation range of Khumbu Glacier whereby a smaller fraction of the glacier relative to total area is located along the zero degree isotherm (e.g., compared to Yala Glacier in Nepal; Immerzeel et al., 2014). Seasonal and daily lapse rates that

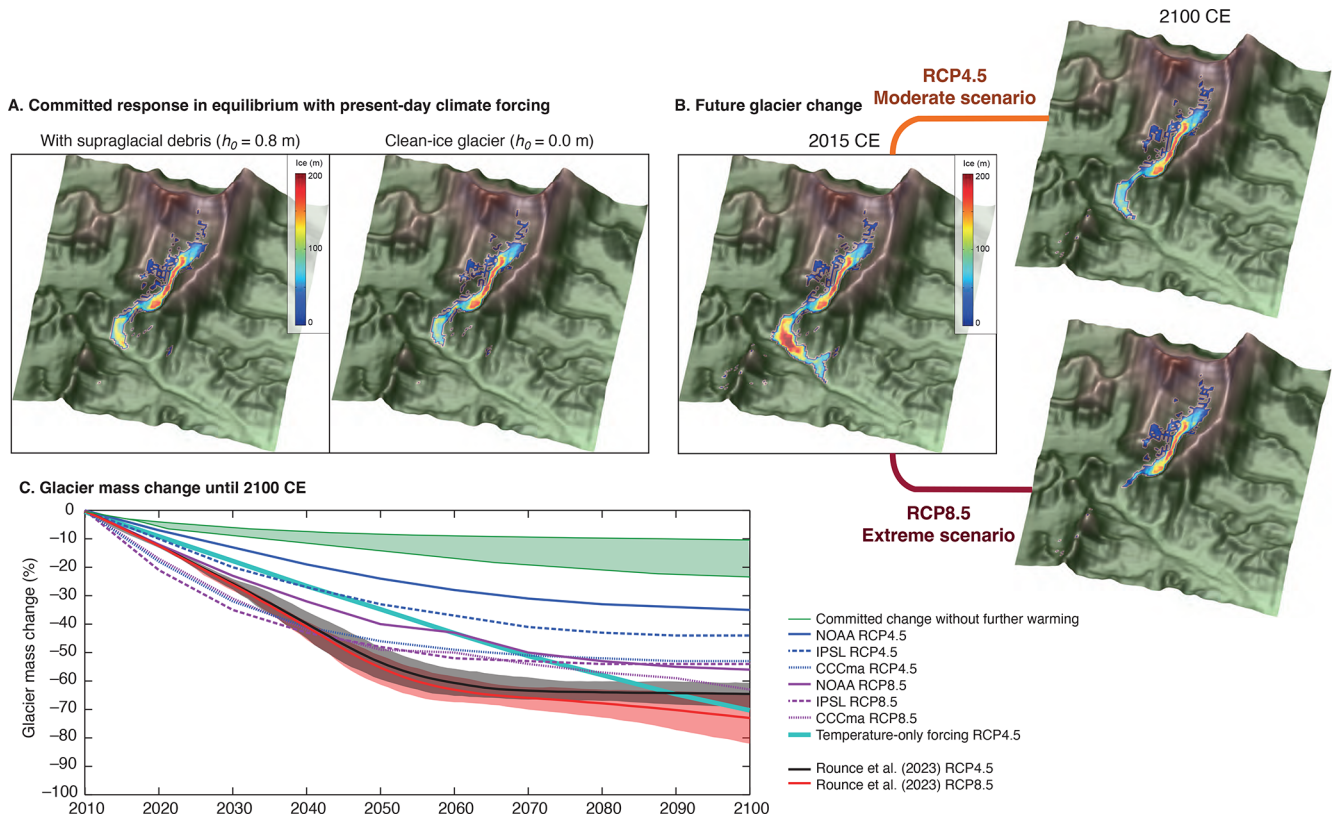


Figure 10. Future glacier volume change projections until 2100 CE. **(a)** Equilibrium ice thickness accounting for the committed response to recent climate change using the downscaled NOAA RCM climate forcing with and without the effect of supraglacial debris on mass balance. **(b)** Simulated ice thickness under RCP4.5 and RCP8.5 for 2100 CE using the downscaled NOAA RCM climate forcing. **(c)** Comparison of projected shrinkage of Khumbu Glacier by 2100 CE from this study with those from Rounce et al. (2023) showing results from each of the six experiments in this study with results from RCP4.5 and RCP8.5 from Rounce et al. (2023), the equivalent result for a simulation using a change in MAAT equivalent to the NOAA RCP4.5 forcing where precipitation does not change from the present-day value (cyan line). The green shading shows the range of the committed volume loss due to historical warming.

accounted for marked lower values during the monsoon season and at night gave a mean annual value of $5.54 \text{ }^\circ\text{C km}^{-1}$, which produced glacier-wide mass balance and ice thickness simulations that were closest to geodetic observations and represented the maximum rates of surface lowering in the upper ablation area where the debris layer is thinnest (Fig. 3D and E).

Sublimation simulated in our study occurred at all elevations with the highest rate of ice loss due to sublimation ($-0.12 \text{ m w.e. a}^{-1}$) in the upper reaches of the Khumbu Glacier catchment near to South Col (about 7495 m a.s.l.) where sublimation dominated ablation with only minor seasonality (Fig. A6). Whilst this amount of ice loss by sublimation is not negligible, it is almost half that found in the point-based calculations after adjusting for the different time periods represented by our studies (Matthews et al., 2020), which is likely due to the assumed uniformity of wind speed across the model domain in COSIPY. Future work to improve the calculation of sublimation in distributed surface mass bal-

ance calculations for high-elevation glaciers would be valuable.

While we have considered the effects of mesoscale meteorology on glacier mass balance, smaller-scale processes operating close to the land surface could also be important. Katabatic winds were suggested to explain a local 15-year decrease in maximum air temperatures and precipitation over glaciers while minimum air temperatures continued to rise (Salerno et al., 2023). However, this effect was found to be short-lived (Shaw et al., 2025) and the impact of microscale near-surface cooling on the duration and extent of mesoscale precipitation and accumulation is likely to be minimal and therefore unlikely to significantly affect glacier-wide mass balance (Mott et al., 2020; Shaw et al., 2024). Observations from the Camp 2 AWS (6464 m a.s.l.) indicate that surface energy fluxes may be sufficient to cause non-negligible melting of glacier surfaces despite freezing air temperatures (Matthews et al., 2020). Results from an ice core from South Col Glacier (>8000 m a.s.l.) combined with COSIPY experiments suggested that ablation may also take place at even at

the highest elevations (Potocki et al., 2022). However, a subsequent study found no evidence of glacier mass change, and identified large uncertainties associated with simulating mass balance at these extreme elevations where sub-daily air temperature gradients and the duration of snow cover strongly affect ablation and accumulation (Brun et al., 2023). Future work is needed to reduce these uncertainties, as very few observations exist of accumulation processes and the upper limit of ablation processes for high-elevation Himalayan glaciers.

4.3 Possible outcomes under RCP8.5

Current global greenhouse gas emissions are following the trajectory of the intermediate emissions scenario RCP4.5, while the high emissions scenario RCP8.5 could be described as “low possibility but high impact” (Pedersen et al., 2020). However, as represented in the RCMs used in our study, mountain regions are warming more rapidly than the global mean such that a global temperature rise of 1.5°C will lead to $2.1 \pm 0.1^{\circ}\text{C}$ of warming in High Mountain Asia (Kraaijenbrink et al., 2017; Pepin et al., 2022) although the occurrence of elevation-dependent warming above 5000 m a.s.l. is debated (Gao et al., 2018). The high temperatures projected under RCP8.5 could potentially be offset partly by increased precipitation, given that high-magnitude precipitation events from winter Westerly disturbances increased by a factor of seven between present day and 2100 CE in the IPSL RCM under RCP8.5.

We found no evidence of future increases in precipitation offsetting RCP8.5 warming; net glacier mass balance was strongly negative in all RCP8.5 experiments and insufficient to maintain any actively flowing glacier. Under RCP8.5, glacier mass balance in the monsoon-influenced Himalaya may therefore shift from being driven by accumulation during the monsoon to predominantly during winter. Monsoon precipitation would only result in snow accumulation at the very highest elevations and would be insufficient to maintain flowing glaciers. This outcome is avoidable by limiting anthropogenic warming to within RCP4.5, which, due to the associated increase in precipitation, could sustain nearly two thirds of the current glacier volume until 2100 CE and potentially for two centuries further into the future.

4.4 Comparison with global glacier modelling results

A recent global glacier modelling study forced by an ensemble of 10 GCMs projected mass loss of 64 % for Khumbu Glacier by 2100 CE (Rounce et al., 2023). In comparison, our experiments project less severe rates of decline, resulting in 30 % less mass loss under the RCP4.5 future climate scenario than in the global study (Fig. 10C). One difference between these results is that rather than using the global glacier inventory outline to define the glacier margins we consider only the actively flowing glacier and so exclude 20 % of the start-

ing glacier volume in the detached tongue. We would expect the two sections of the glacier to evolve along different paths; while the active glacier responds to climate change as projected in our experiments, thick supraglacial debris mantling the detached tongue could allow this ice mass to survive and slowly decay in situ for many decades beyond the present day. The decay of the detached tongue may however increase due to erosion of the surface by ice cliffs and supraglacial water bodies that are expanding across the former glacier surface (King et al., 2020).

Our experiments only consider the rapidly changing active glacier, and we expect that the debris-covered tongue would melt more slowly than projected in the global modelling study, but as we do not consider the stagnant tongue to be part of the present-day glacier the ice volume simulated at the start of our experiments is smaller than that represented by Rounce et al. (2023) and other studies based on the RGI glacier inventory. The dynamically detached debris-covered tongue represents about 20 % of the present-day glacier volume and contains ice estimated as up to 360 m thick. The mean present-day ablation rate across this section of the glacier simulated in Rowan et al. (2021) is $-0.54 \text{ m w.e. a}^{-1}$ which can be used to estimate the life expectancy of the debris-covered tongue assuming no input of ice from the active glacier and no change in ablation rate due to thickening of supraglacial debris or the development of ice cliffs and supraglacial ponds. While the thickest part of the detached tongue may survive for ~ 600 years, the mean life expectancy of this ice mass is 176 ± 148 years from the present day meaning that the former debris-covered tongue will vanish by 2200 CE.

4.5 The response of large debris-covered glaciers to climate change

The dynamic response time of large glaciers to climate change is of the order of centuries. For this reason, we start our simulations from the late Holocene ($\sim 1 \text{ ka}$) moraine extent when Khumbu Glacier was last considered dynamically stable (Hornsey et al., 2022; Rowan et al., 2015). The relationship between glacier response time and mass balance becomes less important after 2100 CE when the glacier is so small that ice flow has little impact on glacier volume change. Global and regional glacier modelling studies typically start their simulations in the current Century (e.g., 2000–2007 CE in Marzeion et al., 2020; 2000 CE in Rounce et al., 2023) and a further complication arises from the use of global glacier inventories as a starting point for glacier modelling studies as such inventories cannot capture the current dynamic state of glaciers that are imbalanced, and include all ice-covered areas rather than identifying only actively flowing ice. However, satellite-derived velocity products could be used identify where ice flow within glacier outlines declines to negligible rates (Dehecq et al., 2019).

The RGI 7.0 inventory for Khumbu Glacier is based on imagery from 1999 CE (RGI 7.0 Consortium, 2023) where the detached debris-covered tongue represents 20 % of the glacier volume contained within this outline (Fig. 1C). Simulations that integrated the stagnant tongue into the model domain rather than as part of the flowing ice improved the representation of simulated ice flow compared to observed values, supporting our conclusion that the debris-covered tongue has been dynamically detached from the active glacier for 50–100 years (Rowan et al., 2021). Field observations support the concept of active and stagnant sections co-existing in contact with each other as englacial optical televiewing indicated that thrusting occurs at several sites, denoted by skewed internal debris layers and of basal ice that has been thrust to the glacier surface, near to the active glacier terminus from the direction of Khumbu Icefall (Miles et al., 2021). Our simulations show that development of supraglacial debris at the active glacier terminus reduced net volume loss by 13 % (Fig. 8). Dynamic detachment of debris-covered tongues could allow these glaciers to move closer to equilibrium with a rapidly changing climate, the local mass balance gradient is a more important control on glacier change for both clean-ice glaciers and debris-covered Himalayan glaciers.

5 Conclusions

In the monsoon-influenced Himalaya, 85 % of the glacier area is located higher than 5000 m above sea level, and 21 % of this ice is above 6000 m in elevation. Despite these high elevations, Himalayan glaciers are rapidly losing ice in response to recent warming and are projected to shrink by 53 % to 70 % during this Century. However, the impact of future changes in precipitation on glacier loss remains uncertain, because changes in precipitation amount and distribution is often overlooked in glacier model projections. We explored the effects of future warming in tandem with changes in precipitation by simulating the evolution of Khumbu Glacier in the Everest region of Nepal using a surface energy and mass balance model forced by downscaled Regional Climate Model outputs to drive an ice-dynamical glacier evolution model. Historical warming commits Khumbu Glacier to loss of 10 %–23 % of the total ice volume by 2100 CE. While warming due to intermediate future greenhouse gas emissions (RCP4.5) will lead to glacier volume loss of 70 % by 2100 CE, the projected concurrent increase in precipitation amount will offset 34 % of this and so reduce glacier loss by about a half. However, high future emissions (RCP8.5) will not be compensated by changes in precipitation amount but will instead result in substantial ablation above 6000 m with devastating consequences for one of the highest glaciers on Earth. Our results indicate that the net mass balance of Khumbu Glacier could be close to zero in 2100 CE under RCP4.5 and therefore, if climate change is limited to this in-

termediate emissions scenario, Khumbu Glacier will recede to the base of the icefall with insignificant further change in glacier volume beyond this point. In this scenario, Khumbu Glacier has a similar extent in 2100 CE to the active section of the present-day glacier, and represents at least one example of how monsoon-influenced Himalayan glaciers could persist into the future if global efforts are sufficient to mitigate anthropogenic climate change.

Appendix A

This appendix contains further details on the meteorological data collection and analysis, RCM downscaling, evaluation of the present-day downscaled RCM results using meteorological data and the distribution of these results across the model domain, and the parameterisation and sensitivity testing of the COSIPY model. The Indian Summer Monsoon season was defined as June to October, the post-monsoon as October–November, winter as December–February, and the pre-monsoon as March–May (Ueno et al., 2008). Although much of this study compares the monsoon season against the non-monsoon season, it should be noted that the timing of monsoon onset and cessation can vary between years. Day time was defined as 08:00–16:00 and night as 20:00–04:00 (Nepal local time) to account for changing sunrise and sunset times throughout the year and the influence of topographic shading in the valleys; centred-means were used for some datasets to remove local noise associated with daily frequencies. For sub-hourly measurements, hourly averages were calculated using data from the previous hour. The period for the reference simulation and sensitivity experiments was 1 January 2013 to 31 December 2015. RCM downscaling to produce the five-year time slices represented the periods 1 January 2015 to 31 December 2019 and 1 January 2095 to 31 December 2099.

A1 Gap filling of the AWS data

All AWS datasets contained periods of erroneous measurements and missing data, which is unsurprising given the challenges of maintaining equipment in such an environment (Oulkar et al., 2026). Daily air temperature averages were calculated when 83 % (20 h) of observations were available. For calculation of lapse rates for longer time periods (e.g. daytimes during the monsoon season) the distributions of missing data across these periods were analysed. For example, the Lukla AWS had almost 45 % of temperature observations missing during the monsoon season but as these were equally distributed between day and night, lapse rates could be calculated using station pairs following the method of Immerzeel et al. (2014). Up to 13 % of the West Changri Nup AWS temperature records were missing, and these were interpolated using the Ev-K2-CNR Pyramid AWS data with the same lapse rate as the GlacioClim dataset. The interpolated

results were compared with the preceding and succeeding periods from the same AWS, and the preceding and succeeding months from other AWS, and compared with data collected in November 2014 at the GlacioClim North Changri Nup AWS (5470 m a.s.l.).

Data gaps in the precipitation datasets were significant, particularly during the onset of the monsoon (e.g., 45 % of data points were missing for the Namche AWS) meaning the altitudinal dependency of precipitation could not be fully characterised. This led to several monsoon seasons with little or no data at individual AWS. Given that the aim of this study was to analyse in situ trends, gap-filling through interpolation was not conducted for these AWS during the seasons without data. Station pairs were used to determine the elevation dependency of precipitation for the reference simulation following the method of Immerzeel et al. (2014). Results from the Kala Patthar/Pheriche station pair and the Pyramid/Pheriche station pair in 2009, and the Kala Patthar/Namche station pair during 2011, show that the relationship between precipitation amount and elevation was more negative during the monsoon season ($-0.011\% \text{ m}^{-1}$ to $-0.018\% \text{ m}^{-1}$) than during the non-monsoon ($-0.0039\% \text{ m}^{-1}$ to $-0.0043\% \text{ m}^{-1}$). No interpolation to fill data gaps was required for other meteorological variables, apart from albedo but as this was only measured at the West Changri Nup AWS there was no suitable surrogate for this variable.

A2 Downscaled climate model results compared with observations

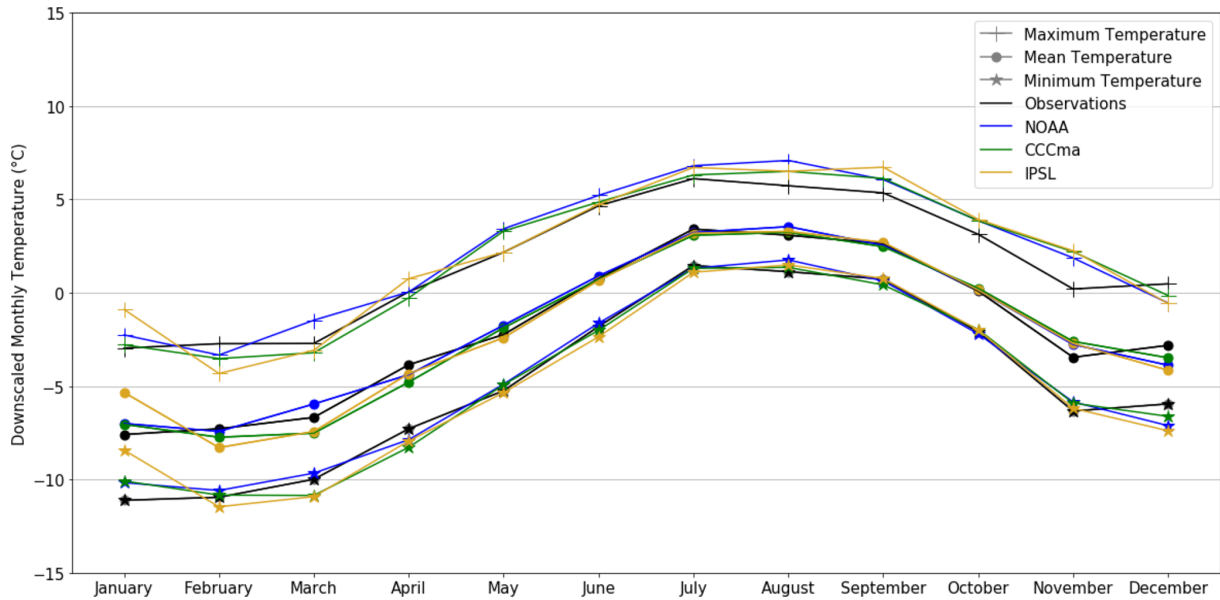


Figure A1. Downscaled monthly mean, maximum, and minimum temperature calculated for the present day time slice compared with observations from the GlacioClim Pyramid Observatory AWS.

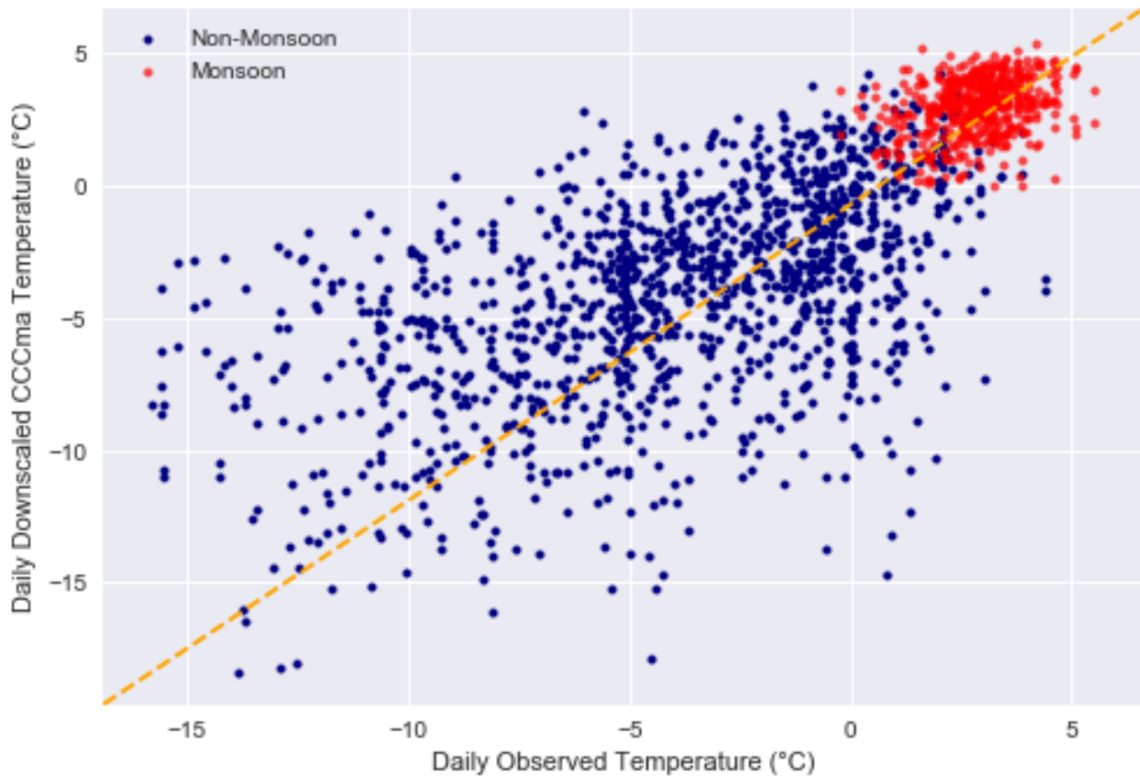


Figure A2. Daily downscaled temperature from the NOAA RCM against observations from the GlacioClim Pyramid Observatory AWS split by monsoon/non-monsoon. The 1 : 1 relationship is shown by the dashed orange line.

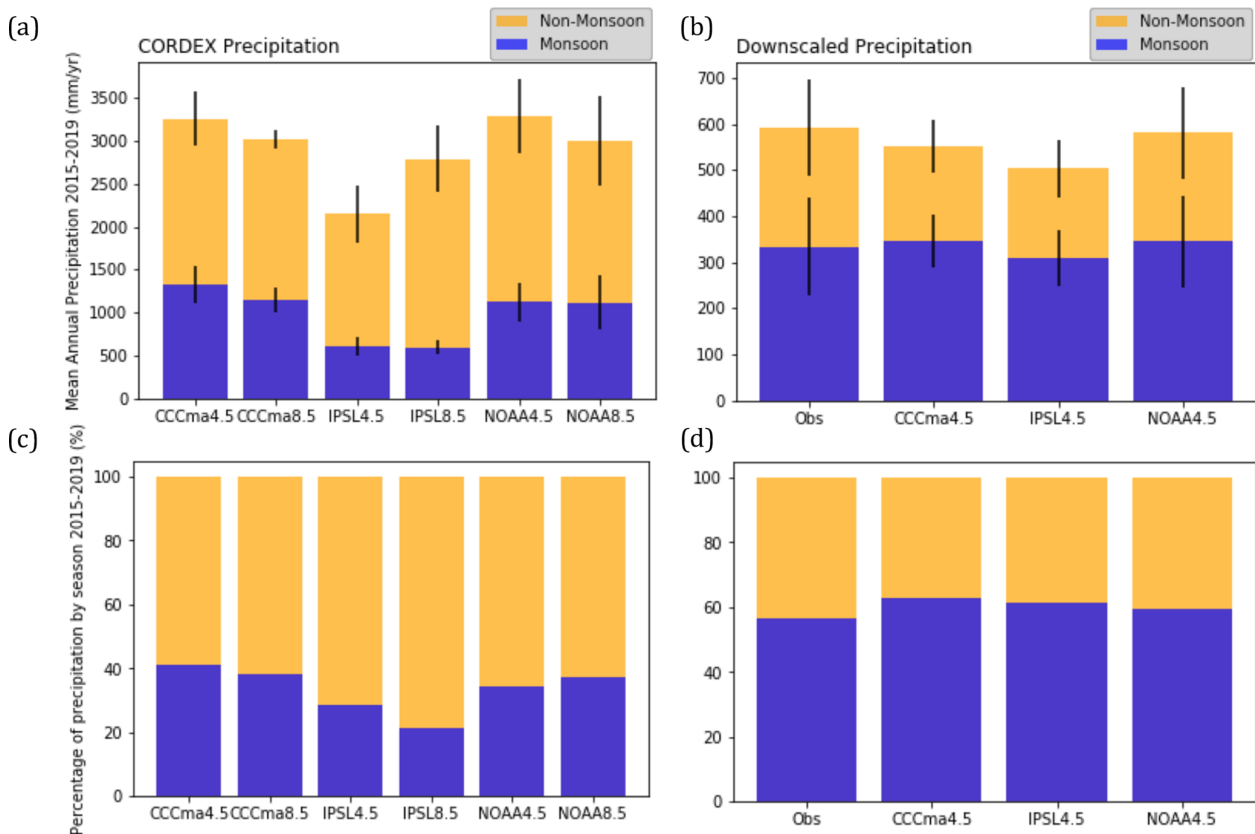


Figure A3. Annual precipitation totals for the monsoon and non-monsoon seasons. **(a and b)** Precipitation totals before and after downscaling, with the standard deviation between selected years shown by black bars. **(c and d)** The same results as seasonal percentages. The annual precipitation is in good agreement with measurements in the southern Dudh Koshi catchment for the gridbox nearest to Khumbu Glacier is located at 27.9065056° N, 86.4352951° E at 2100 m a.s.l.

A3 Regional Climate Model analysis and selection

Three of the six available CORDEX South Asia RCMs (NOAA, CCCma, IPSL) were selected as discrete scenarios that spanned the range of possible future precipitation conditions (Table 1); either wet, moderate, or dry climate in 2080–2100 CE (Fig. A4). The raw RCMs significantly overestimated the annual total precipitation by at least a factor of five for the selected gridpoint, which was corrected by downscaling of these results using the AWS data.

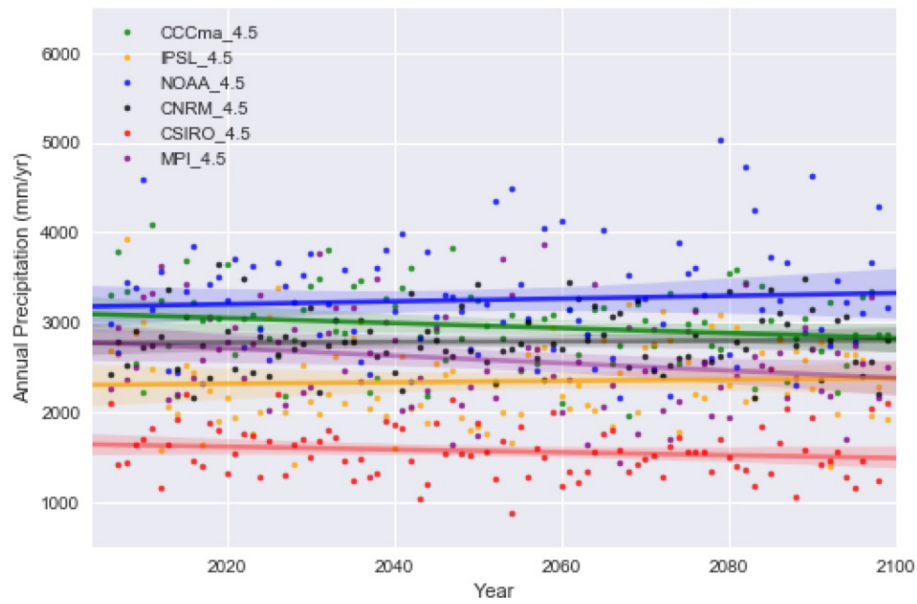


Figure A4. Annual precipitation sums (dots) with fitted trend line from the start of the RCP experiments (2006–2100 CE) for each of the six Indian Institute for Tropical Meteorology CORDEX models for RCP4.5.

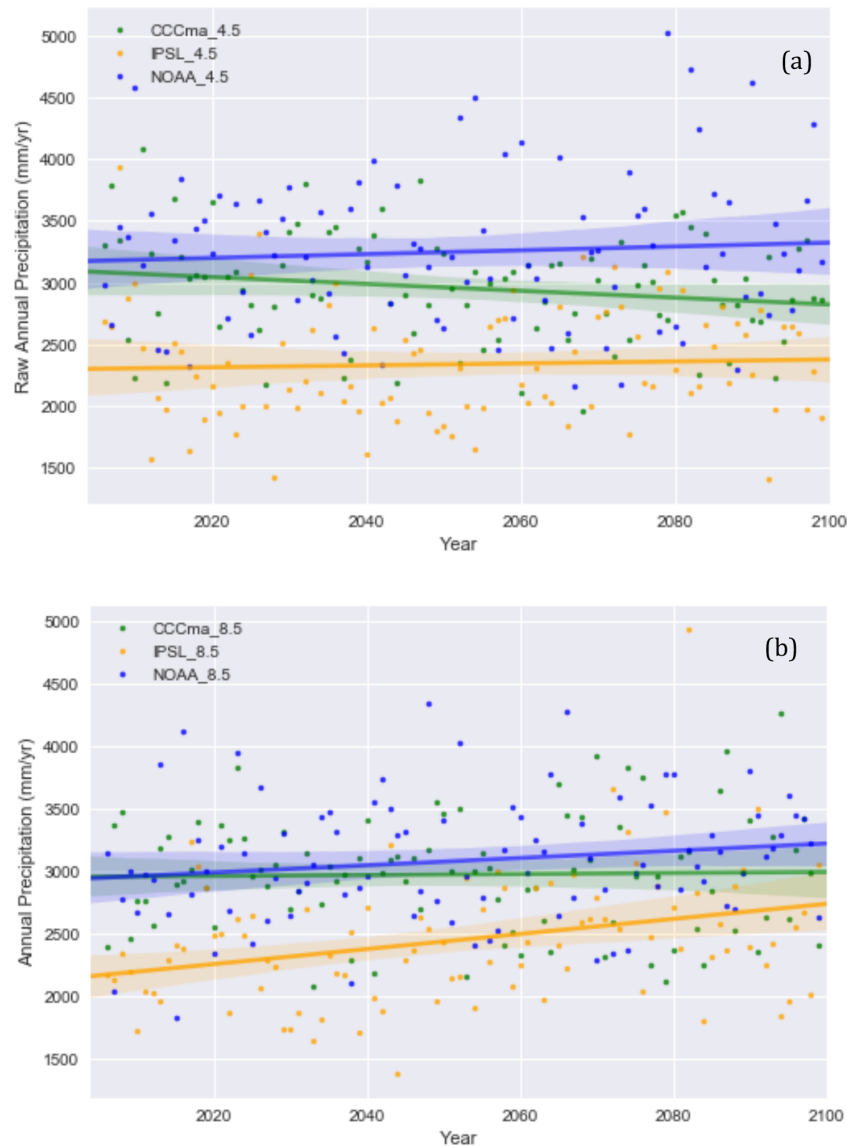


Figure A5. Annual precipitation sums (dots) with fitted trend line from the start of the RCP experiments (2006–2100 CE) for the three selected of the six CORDEX models for (a) RCP4.5 and (b) RCP8.5.

A4 Downscaling parameters and method

While minimum and maximum air temperatures are not required to as inputs to COSIPY, these were downloaded and statistically downscaled using quantile mapping with normal distribution to aid disaggregation to an hourly time step using MELODIST (Table A1). Quantile mapping for the CORDEX wind speed data was found to be ineffective when analysing the time series output against observations, both for the absolute wind speed as well as the reduced day-on-day variability seen during the monsoon season, and therefore, GARD was used instead. This is a simple statistical analogue regression downscaling method appropriate for pointwise downscaling.

Table A1. RCM-derived parameters and the method used for downscaling or bias correction.

RCM-derived parameters	Downscaling/bias correction method	Parametric distribution model (for Quantile mapping)	References
Precipitation ($\text{kg m}^{-2} \text{s}^{-1}$, converted to mm d^{-1})	Quantile mapping	Gamma	Vrac et al. (2007); Piani et al. (2010)
Mean temperature (K) Minimum temperature (K) Maximum temperature (K)	Quantile mapping	Normal/Gaussian	Li et al. (2010); Gupta and Tarboton (2016); Luo et al. (2018)
Incoming shortwave (W m^{-2}) Incoming longwave (W m^{-2}) Relative humidity (%)	Quantile mapping	Beta	Ruane et al. (2015)
Pressure (hPa)	Bias correction	Not applicable	Not applicable
Wind speed (m s^{-1})	Regression downscaling	Not applicable	Gutmann et al. (2022)

A5 Variability in surface energy balance with elevation

The contributions of the components of the surface energy balance were tested at five points along the glacier centre-line (Fig. 5) and found to vary substantially in both absolute values and seasonality. Net shortwave radiation (Q_{SW}) contributed the largest energy input to the glacier surface at the lower elevation sites and correlated most strongly with Q_{melt} . The high temporal variability related to varied cloud cover and fluctuating albedo during the warmer months with the melting of the snowpack. Q_{SW} was low at higher elevations, but high SW_{in} at the higher sites indicates that this is not due to topographic shading. Q_{SW} is correlated with albedo, and the persistence of snow throughout much of the year will reduce Q_{melt} . Q_{LW} rose above zero during the monsoon season at sites EB5950, EB6480 and EB7910, mostly due to heavy cloud cover and increased temperatures relative to the glacier surface. Q_{lat} was close to zero at the lower elevation sites as the arrival of the monsoon led to higher relative humidity, and this pattern was similar but dampened at higher elevations. At the highest site, EB7910, Q_{melt} correlated exactly with the sensible heat flux.

Sublimation occurred at all elevations, with the highest cumulative loss at EB7910 (Fig. A6A). Sublimation rates correlated with seasonality down-glacier; at EB7910 sublimation only slightly slowed from December until May, while sublimation at site EB4980 increased from April until the start of the monsoon in July. Subsurface melt at or above the ELA (5950 m a.s.l.) was negligible, but lower elevation sites showed stronger seasonal cycles related to surface temperatures. Refreezing (Fig. A6C) occurred at all sites and the onset of refreezing was staggered with increasing elevation, although absolute values remained low. Higher Q_{lat} during the monsoon resulted in higher deposition of snow to the glacier at lower elevations and negligible rates at higher elevations. Similar absolute values and patterns are seen for condensation (results not shown).

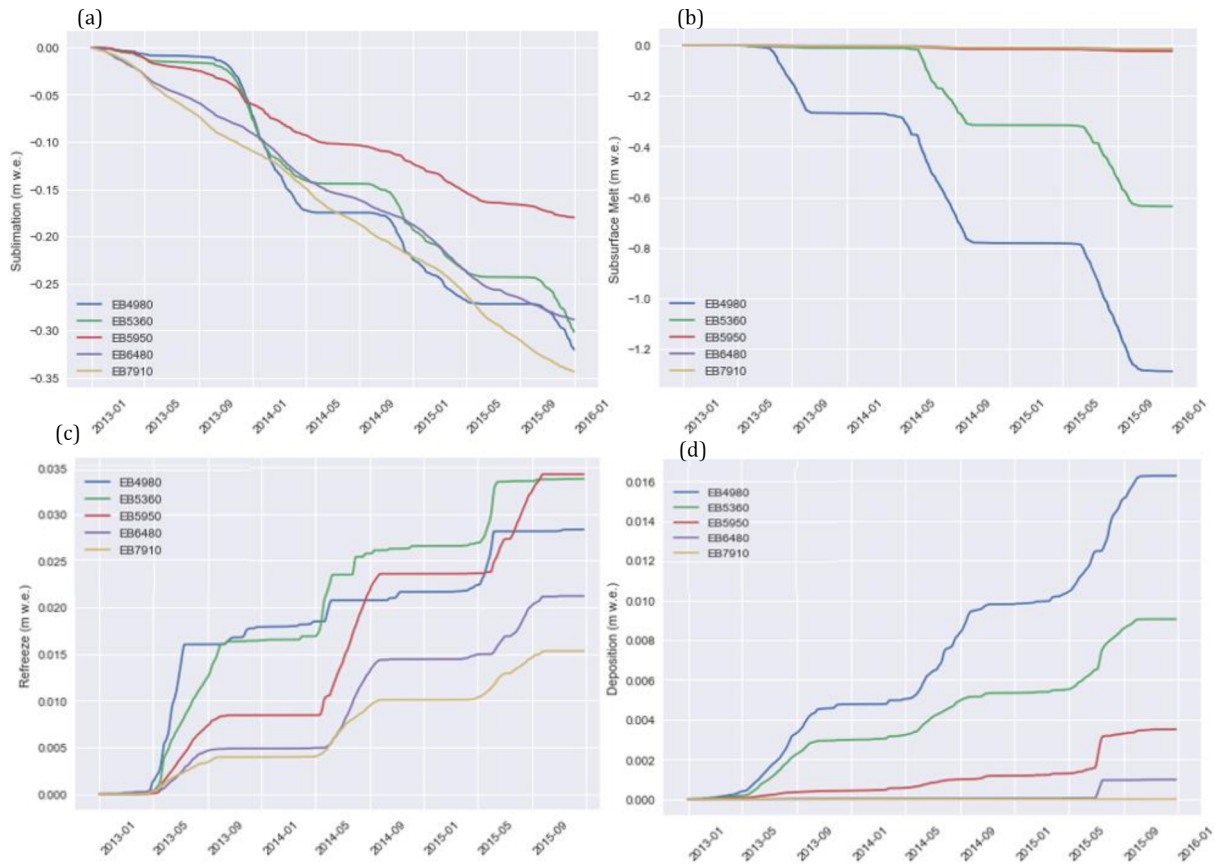


Figure A6. 5 d averages of (a) sublimation, (b) subsurface melt, (c) refreeze, and (d) deposition for the five surface energy balance sensitivity testing sites across Khumbu Glacier (see Fig. 5 for locations of these sites).

A6 COSIPY parameter testing and sensitivity results

To isolate the impact of individual surface energy balance variables on the mass balance of Khumbu Glacier, each variable was perturbed individually, and air temperature and precipitation amount were tested in tandem for the reference period 2013–2015 CE (Table A2). Perturbations of all variables were within the range of possible uncertainty that arise from a combination of observations, climate models, down-scaling approach or the distribution of meteorology. The positive temperature and precipitation perturbations were in the order of possible future climate forcings. The spatially averaged mass balance was most sensitive to changes in LW_{in} , air temperature, and SW_{in} , and relative humidity had the least impact on ablation/accumulation rates (Fig. A7). The coupled parameter testing (Fig. A8) perturbed precipitation and air temperature simultaneously. The most significant change in spatially averaged mass balance followed a 3 °C increase in air temperature and 20 % decrease in precipitation amount. The increase in ablation following an increase in air temperature of 1.5 °C was completely compensated by the increase in accumulation resulting from a 20 % increase in precipitation amount.

Accurate estimation of precipitation phase is important for summer-accumulation type glaciers and threshold values of air temperature are often used to separate liquid and solid precipitation. Previous work calculated threshold temperatures across 6883 AWS in the Northern Hemisphere to find an average rain/snow partitioning value of 1 °C, with 95 % of observations falling between 0.4 and 2.4 °C (Jennings et al., 2018). Although there remains a lack of such data for High Mountain Asia, Jennings et al. (2018) found that high mountain areas have the highest rain/snow partitioning thresholds, with a value of up to 4.5 °C on the Tibetan Plateau. The impact of two different precipitation partitioning schemes on glacier mass balance was investigated here. Threshold temperatures of 0.5, 2.0 and 3.5 °C were chosen and compared with the default value in COSIPY (STF), and a scheme that smoothly scaled from 100 % solid precipitation at −1 °C to 0 % solid precipitation at 4 °C was also tested.

The glacier ice surface roughness (z_0) was defined as 1.7 mm for the reference simulation, which is a reasonable estimate for clean-ice glaciers (Mölg et al., 2012). The z_0 values reported within the literature vary widely for clean-ice glaciers, and two substantially different z_0 values were tested. A z_0 value of 0.1 mm was measured at Midtre Lovén-

Table A2. Parameter perturbations for the sensitivity experiments. Note that for relative humidity the % refers to the units and not the perturbation.

Parameter	Perturbation
Mean annual air temperature (°C)	$\pm 1.5, \pm 2.0, \pm 3.0$
Precipitation amount (%)	$\pm 10, \pm 20, \pm 30$
Wind speed (m s^{-1})	$\pm 0.75, \pm 1.5$
SW_{in} and LW_{in} (%)	$\pm 10, \pm 20$
Relative Humidity (%)	$\pm 10, \pm 20$

breed, Svalbard (Irvine-Fynn et al., 2014), and August-One glacier, China (Guo et al., 2018), and a z_0 value of 6.9 mm was calculated on the clean-ice section of the Haut Glacier D’Arolla (Brock et al., 2006) and Laohugou Glacier No. 12 (Sun et al., 2018). These values were used as endmembers of the likely range in values for Khumbu Glacier. The z_0 value had minimal impact on glacier mass balance (Fig. A9) although a higher (lower) value for z_0 did result in slightly increased (decreased) mass balance. The mass balance sensitivity was not proportional to the change in z_0 , with a z_0 value of 1.6 mm lower than the reference value leading to a similar mass balance change than that of the experiment with a z_0 value of 5.2 mm higher than the reference value.

The albedo values of the three glacier components were perturbed by ± 0.05 from that used in the reference experiment (e.g., 0.85 for fresh snow). There was a strong response of the glacier mass balance to changing snow albedo. Reducing snow albedo by 0.05 led to a 65 % reduction in mass balance of 2.21 m w.e. (Fig. A9). Ablation (accumulation) rates were 3.7 m w.e. (1.75 m w.e.) higher relative to the reference simulation for this perturbation. This result further supports the importance of Q_{SW} to ablation rates. Varying albedo values for firn and ice also revealed a lower sensitivity of glacier mass balance relative to snow albedo.

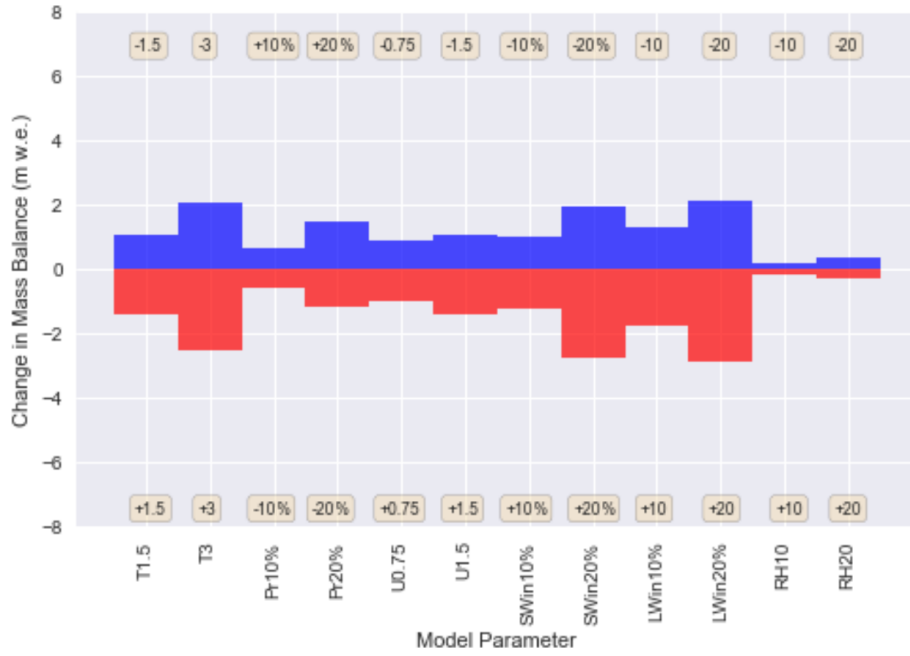


Figure A7. Single parameter sensitivity test results for reference simulation period 2013–2015 CE.

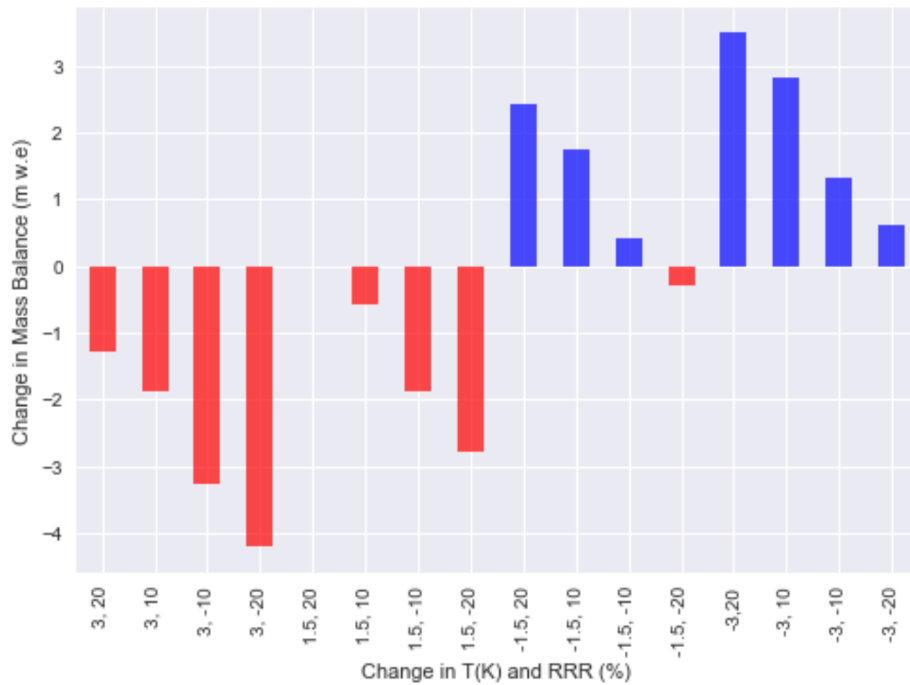


Figure A8. Coupled parameter sensitivity test results for mean annual air temperature and precipitation amount for reference simulation period 2013–2015 CE.

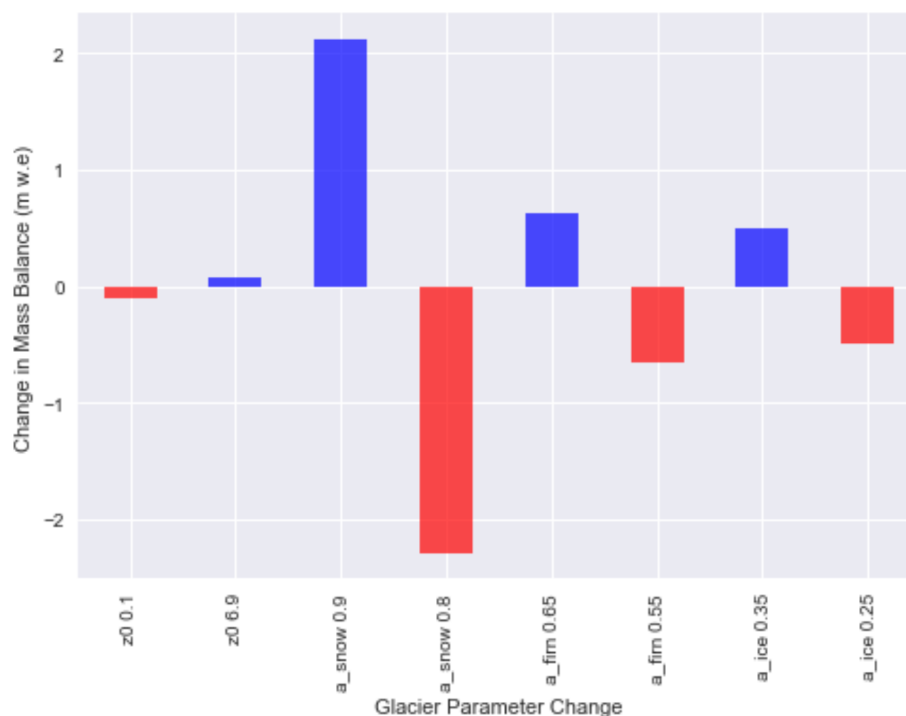


Figure A9. Sensitivity of mass balance for the reference simulation period 2013–2015 CE to changing glacier parameters (surface roughness, and albedo of snow, firm, and ice).

Code availability. The COSIPY version 1.3 glacier surface energy and mass balance model is available from the original publication describing this model (Sauter et al., 2020) and Zenodo (<https://doi.org/10.5281/zenodo.3902191>, Arndt et al., 2020). The iSOSIA version spm-3.3.3r glacier model is available from Zenodo (<https://doi.org/10.5281/zenodo.12666864>, Rowan and Pedersen, 2024).

Data availability. Daily data from the Coordinated Regional Downscaling Experiment (CORDEX) South Asia domain were downloaded from the Indian Institute of Tropical Meteorology website (<https://cccr.tropmet.res.in/cordex-sa/cordexsa-data.php>, last access: 18 May 2026) for the grid box nearest to Khumbu Glacier (27.9065°N, 86.4353°E). Incoming shortwave and longwave radiation components were downloaded from the ESGF portal (<https://cordex.org/data-access/cordex-cmip5-data/cordex-cmip5-simulations/>, last access: 18 May 2026). Meteorological observations were derived from the EvK2-CNR SHARE network (<https://www.ev2cnr.org>, last access: 18 May 2026) and the GlacioClim (<https://glacioclim.osug.fr/Donnees-du-Nepal-region-du-Khumbu>, last access: 18 May 2026).

Author contributions. Conceptualisation: DJQ, ANR, AVR. Data curation: ASD, ANR, AVR. Formal analysis: ASD, ANR, AVR. Funding acquisition: DJQ, ANR, AVR. Investigation: ASD. Methodology: ASD, ANR, AVR, VKP. Project administration: DJQ, ANR. Resources: DJQ, ANR. Software: AVR, VKP. Supervision: DJQ, ANR, AVR. Validation: ASD, AVR. Visualisation: ASD, AVR. Writing – original draft preparation: ASD, AVR, DJQ, ANR, VKP. Writing – review and editing: ASD, AVR, DJQ, ANR, VKP.

Competing interests. The contact author has declared that none of the authors has any competing interests.

Disclaimer. Publisher's note: Copernicus Publications remains neutral with regard to jurisdictional claims made in the text, published maps, institutional affiliations, or any other geographical representation in this paper. The authors bear the ultimate responsibility for providing appropriate place names. Views expressed in the text are those of the authors and do not necessarily reflect the views of the publisher.

Acknowledgements. Tobias Sauter and Anselm Arndt are thanked for support in using COSIPY. We thank Patrick Wagnon for sharing the Pyramid and Changri Nup Glacier automatic weather station data. We thank David Rounce for sharing the global glacier model results for Khumbu Glacier from Rounce et al. (2023).

Financial support. ASD was supported by the Priestley International Centre for Climate at the University of Leeds, and a University of Leeds Anniversary Research Scholarship. AVR was supported by a Royal Society Dorothy Hodgkin Research Fellowship (DHF\R1\201113). Some of the simulations presented were performed using resources provided by Sigma2, the National Infrastructure for High-Performance Computing and Data Storage in Norway.

Review statement. This paper was edited by Emily Collier and reviewed by Emily Potter and two anonymous referees.

References

- Ageta, Y.: Characteristics of precipitation during monsoon season in Khumbu Himalaya, *Seppyo*, 38, 84–88, https://doi.org/10.5331/seppyo.38.Special_84 (last access: 18 May 2026), 1976.
- Altena, B. and Kääb, A.: Ensemble matching of repeat satellite images applied to measure fast-changing ice flow, verified with mountain climber trajectories on Khumbu icefall, Mount Everest, *J. Glaciol.*, 66, 905–915, <https://doi.org/10.1017/jog.2020.66>, 2020.
- Anderson, L. S. and Anderson, R. S.: Modeling debris-covered glaciers: response to steady debris deposition, *The Cryosphere*, 10, 1105–1124, <https://doi.org/10.5194/tc-10-1105-2016>, 2016.
- Arndt, A., Sauter, T., and Saß, B.: cryotools/cosipy: COSIPY v1.3 – An open-source coupled snowpack and ice surface energy and mass balance model (v1.3), Zenodo [code], <https://doi.org/10.5281/zenodo.3902191>, 2020.
- Bartlett, O. T., Ng, F. S. L., and Rowan, A. V.: Morphology and evolution of supraglacial hummocks on debris-covered Himalayan glaciers, *Earth Surf. Process. Landforms*, 46, 525–539, <https://doi.org/10.1002/esp.5043>, 2021.
- Benn, D. I. and Lehmkuhl, F.: Mass balance and equilibrium-line altitudes of glaciers in high-mountain environments, *Quatern. Int.*, 65–66, 15–29, [https://doi.org/10.1016/S1040-6182\(99\)00034-8](https://doi.org/10.1016/S1040-6182(99)00034-8), 2000.
- Benn, D. I. and Owen, L. A.: The role of the Indian summer monsoon and the mid-latitude westerlies in Himalayan glaciation: review and speculative discussion, *Journal of the Geological Society*, 155, 353–363, <https://doi.org/10.1144/gsjgs.155.2.0353>, 1998.
- Biemans, L. H., Speelman, F., Ludwig, E. J., Moors, A. J., Wiltshire, P., Kumar, D., Gerten, P., and Kabat, P.: Future water resources for food production in five South Asian river basins and potential for adaptation – A modeling study, *Sci. Total Environ.*, <https://doi.org/10.1016/j.scitotenv.2013.05.092>, 2013.
- Bollasina, M., Bertolani, L., and Tartari, G.: Meteorological observations at high altitude in the Khumbu Valley, Nepal Himalayas, 1994–1999, *Bull. Glaciol. Res.*, 19, 1–11, https://www.seppyo.org/publication/bgr/archive/bgr_19_2002/attachment/bgr19p1/ (last access: 18 May 2026), 2002.
- Bonekamp, P. N. J., Wanders, N., Wiel, K., Lutz, A. F., and Immerzeel, W. W.: Using large ensemble modelling to derive future changes in mountain specific climate indicators in a 2 and 3 °C warmer world in High Mountain Asia, *Int. J. Climatol.*, 41, <https://doi.org/10.1002/joc.6742>, 2021.
- Bookhagen, B. and Burbank, D. W.: Topography, relief, and TRMM-derived rainfall variations along the Himalaya, *Geophys. Res. Lett.*, 33, L08405, <https://doi.org/10.1029/2006GL026037>, 2006.
- Brock, B. W., Willis, I. C., and Sharp, M. J.: Measurement and parameterization of aerodynamic roughness length variations at Haut Glacier d’Arolla, Switzerland, *J. Glaciol.*, 52, 281–297, <https://doi.org/10.3189/172756506781828746>, 2006.
- Brun, F., King, O., Réveillet, M., Amory, C., Planchot, A., Berthier, E., Dehecq, A., Bolch, T., Fourteau, K., Brondex, J., Dumont, M., Mayer, C., Leinss, S., Hugonnet, R., and Wagnon, P.: Everest South Col Glacier did not thin during the period 1984–2017, *The Cryosphere*, 17, 3251–3268, <https://doi.org/10.5194/tc-17-3251-2023>, 2023.
- Collins, M., Knutti, R., and Arblaster, J.: Long-term Climate Change: Projections, Commitments and Irreversibility, in: *Climate Change 2013: The Physical Science Basis. Contribution of Working Group I to the Fifth Assessment Report of the Intergovernmental Panel on Climate Change*, edited by: Stocker, T. F., Qin, D., Plattner, G.-K., Tignor, M., Allen, S. K., Boschung, J., Nauels, A., Xia, Y., Bex V., and Midgley, P. M., Cambridge University Press, Cambridge, United Kingdom and New York, NY, USA, 1–108, https://www.ipcc.ch/site/assets/uploads/2018/02/WG1AR5_Chapter12_FINAL.pdf (last access: 18 May 2026), 2013.
- Compagno, L., Huss, M., Miles, E. S., McCarthy, M. J., Zekolari, H., Dehecq, A., Pellicciotti, F., and Farinotti, D.: Modelling supraglacial debris-cover evolution from the single-glacier to the regional scale: an application to High Mountain Asia, *The Cryosphere*, 16, 1697–1718, <https://doi.org/10.5194/tc-16-1697-2022>, 2022.
- Cuffey, K. M. and Paterson, W. S. B.: *The physics of glaciers*, 4th edn., Academic Press, 704 pp., ISBN-10: 0-123694-61-2, ISBN-13: 978-0-123-69461-4, 2010.
- Dehecq, A., Gourmelen, N., Gardner, A. S., Brun, F., Goldberg, D., Nienow, P. W., Berthier, E., Vincent, C., Wagnon, P., and Trouvé, E.: Twenty-first century glacier slowdown driven by mass loss in High Mountain Asia, *Nat. Geosci.*, 12, 22–27, <https://doi.org/10.1038/s41561-018-0271-9>, 2019.
- Egholm, D. L., Knudsen, M. F., Clark, C. D., and Lesemann, J. E.: Modeling the flow of glaciers in steep terrains: The integrated second-order shallow ice approximation (iSOSIA), *J. Geophys. Res.*, 116, <https://doi.org/10.1029/2010JF001900>, 2011.
- Farinotti, D., Huss, M., Fürst, J. J., Landmann, J., Machguth, H., Maussion, F., and Pandit, A.: A consensus estimate for the ice thickness distribution of all glaciers on Earth, *Nat. Geosci.*, 12, 168–173, <https://doi.org/10.1038/s41561-019-0300-3>, 2019.
- Farr, T. G., Rosen, P. A., Caro, E., Crippen, R., Duren, R., Hensley, S., Kobrick, M., Paller, M., Rodriguez, E., Roth, L., Seal, D., Shaffer, S., Shimada, J., Umland, J., Werner, M., Oskin, M., Burbank, D., and Alsdorf, D.: The Shuttle Radar Topography Mission, *Rev. Geophys.*, 45, 2005RG000183, <https://doi.org/10.1029/2005RG000183>, 2007.
- Ferguson, J. C. and Vieli, A.: Modelling steady states and the transient response of debris-covered glaciers, *The Cryosphere*, 15, 3377–3399, <https://doi.org/10.5194/tc-15-3377-2021>, 2021.
- Förster, K., Hanzer, F., Winter, B., Marke, T., and Strasser, U.: An open-source MEteoroLOGical observation time series DISaggre-

- gation Tool (MELODIST v0.1.1), *Geosci. Model Dev.*, 9, 2315–2333, <https://doi.org/10.5194/gmd-9-2315-2016>, 2016.
- Gades, A., Conway, H., Nereson, N., Naito, N., and Kadota, T.: Radio echo-sounding through supraglacial debris on Lirung and Khumbu Glaciers, Nepal Himalayas, *Debris-Covered Glaciers* (Proceedings of a workshop held at Seattle, Washington, USA, September 2000), IAHS, 264, 13–22, ISBN-10: 1901502317, ISBN-13: 978-1901502312., 2000.
- Gao, Y., Chen, F., Lettenmaier, D. P., Xu, J., Xiao, L., and Li, X.: Does elevation-dependent warming hold true above 5000 m elevation? Lessons from the Tibetan Plateau, *npj Clim. Atmos. Sci.*, 1, 19, <https://doi.org/10.1038/s41612-018-0030-z>, 2018.
- Gromke, C., Manes, C., Walter, B., Lehning, M., and Guala, M.: Aerodynamic roughness length of fresh snow, *Bound.-Lay. Meteorol.*, 141, 21–34, <https://doi.org/10.1007/s10546-011-9623-3>, 2011.
- Guo, S., Chen, R., Liu, G., Han, C., Song, Y., Liu, J., Yang, Y., Liu, Z., Wang, X., Liu, X., and Wang, L.: Simple parameterization of aerodynamic roughness lengths and the turbulent heat fluxes at the top of midlatitude August-One Glacier, Qilian Mountains, China, *J. Geophys. Res.-Atmos.*, 123, 12066–12080, <https://doi.org/10.1029/2018JD028875>, 2018.
- Gupta, A. and Tarboton, D. G.: A tool for downscaling weather data from large-grid reanalysis products to finer spatial scales for distributed hydrological applications, *Environ. Modell. Softw.*, 84, 50–69, <https://doi.org/10.1016/j.envsoft.2016.06.014>, 2016.
- Gutmann, E. D., Hamman, J. J., Clark, M. P., Eidhammer, T., Wood, A. W., and Arnold, J. R.: En-GARD: A Statistical Downscaling Framework to Produce and Test Large Ensembles of Climate Projections, *J. Hydrometeorol.*, 23, 1545–1561, <https://doi.org/10.1175/JHM-D-21-0142.1>, 2022.
- Herreid, S. and Pellicciotti, F.: The state of rock debris covering Earth's glaciers, *Nat. Geosci.*, 13, 621–627, <https://doi.org/10.1038/s41561-020-0615-0>, 2020.
- Hornsey, J., Rowan, A. V., Kirkbride, M. P., Livingstone, S. J., Fabel, D., Rodes, A., Quincey, D. J., Hubbard, B., and Jomelli, V.: Be-10 Dating of Ice-Marginal Moraines in the Khumbu Valley, Nepal, Central Himalaya, Reveals the Response of Monsoon-Influenced Glaciers to Holocene Climate Change, *J. Geophys. Res.-Earth*, 127, <https://doi.org/10.1029/2022JF006645>, 2022.
- Huintjes, E., Neckel, N., Hochschild, V., and Schneider, C.: Surface energy and mass balance at Purogangri ice cap, central Tibetan Plateau, 2001–2011, *J. Glaciol.*, 61, 1048–1060, <https://doi.org/10.3189/2015JoG15J056>, 2015.
- Immerzeel, W. W., van Beek, L. P. H., Konz, M., Shrestha, A. B., and Bierkens, M. F. P.: Hydrological response to climate change in a glacierized catchment in the Himalayas, *Climatic Change*, 110, 721–736, <https://doi.org/10.1007/s10584-011-0143-4>, 2012.
- Immerzeel, W., Petersen, L., Ragetti, S., and Pellicciotti, F.: The importance of observed gradients of air temperature and precipitation for modeling runoff from a glacierized watershed in the Nepalese Himalayas, *Water Resour. Res.*, 50, 2212–2226, <https://doi.org/10.1002/2013WR014506>, 2014.
- Irvine-Fynn, T. D., Sanz-Ablanedo, E., Rutter, N., Smith, M. W., and Chandler, J. H.: Measuring glacier surface roughness using plot-scale, close-range digital photogrammetry, *J. Glaciol.*, 60, 957–969, <https://doi.org/10.3189/2014JoG14J032>, 2014.
- Jennings, K. S., Winchell, T. S., Livneh, B., and Molotch, N. P.: Spatial variation of the rain–snow temperature threshold across the Northern Hemisphere, *Nat. Commun.*, 9, 1148, <https://doi.org/10.1038/s41467-018-03629-7>, 2018.
- Jouvet, G., Huss, M., Funk, M., and Blatter, H.: Modelling the retreat of Grosse Aletschgletscher, Switzerland, in a changing climate, *J. Glaciol.*, 57, 1033–1045, <https://doi.org/10.3189/002214311798843359>, 2011.
- Kaini, S., Nepal, S., Pradhananga, S., Gardner, T., and Sharma, A. K.: Representative general circulation models selection and downscaling of climate data for the transboundary Koshi river basin in China and Nepal, *Int. J. Climatol.*, 40, 4131–4149, <https://doi.org/10.1002/joc.6447>, 2019.
- Katzenberger, A., Schewe, J., Pongratz, J., and Levermann, A.: Robust increase of Indian monsoon rainfall and its variability under future warming in CMIP6 models, *Earth Syst. Dynam.*, 12, 367–386, <https://doi.org/10.5194/esd-12-367-2021>, 2021.
- Khadka, A., Matthews, T., Perry, L. B., Koch, I., Wagnon, P., Shrestha, D., Sherpa, T. C., Aryal, D., Tait, A., Sherpa, T. G., Tuladhar, S., Baidya, S. K., Elvin, S., Elmore, A. C., Gajurel, A., and Mayewski, P. A.: Weather On Mount Everest During The 2019 Summer Monsoon, *Weather*, 76, 205–207, <https://doi.org/10.1002/wea.3931>, 2021.
- King, O., Bhattacharya, A., Ghuffar, S., Tait, A., Guilford, S., Elmore, A. C., and Bolch, T.: Six Decades of Glacier Mass Changes around Mt. Everest Are Revealed by Historical and Contemporary Images, *One Earth*, 3, 608–620, <https://doi.org/10.1016/j.oneear.2020.10.019>, 2020.
- Knap, W. H. and Oerlemans, J.: The surface albedo of the Greenland ice sheet: satellite-derived and in situ measurements in the Søndre Strømfjord area during the 1991 melt season, *J. Glaciol.*, 42, 364–374, <https://doi.org/10.3189/S0022143000004214>, 1996.
- Kneib, M., Maussion, F., Brun, F., Carcanade, G., Farinotti, D., Huss, M., Van Tiel, M., Jouberton, A., Schmitt, P., Schuster, L., Dehecq, A., and Champollion, N.: Topographically-controlled contribution of avalanches to glacier mass balance in the 21st century, *Nat. Commun.*, 16, 10122, <https://doi.org/10.1038/s41467-025-65608-z>, 2025.
- Kraaijenbrink, P. D. A., Bierkens, M. F. P., Lutz, A. F., and Immerzeel, W. W.: Impact of a global temperature rise of 1.5 degrees Celsius on Asia's glaciers, *Nature*, 549, 257–260, <https://doi.org/10.1038/nature23878>, 2017.
- Lafon, T., Dadson, S., Buys, G., and Prudhomme, C.: Bias correction of daily precipitation simulated by a regional climate model: a comparison of methods, *Int. J. Climatol.*, 33, 1367–1381, 2013.
- Laha, S., Kumari, R., Singh, S., Mishra, A., Sharma, T., Banerjee, A., Nainwal, H. C., and Shankar, R.: Evaluating the contribution of avalanching to the mass balance of Himalayan glaciers, *Ann. Glaciol.*, 58, 110–118, <https://doi.org/10.1017/aog.2017.27>, 2017.
- Lente, G. and Ósz, K.: Barometric formulas: various derivations and comparisons to environmentally relevant observations, *ChemTexts*, 6, 1–14, <https://doi.org/10.1007/s40828-020-0111-6>, 2020.
- Li, H., Sheffield, J., and Wood, E. F.: Bias correction of monthly precipitation and temperature fields from Intergovernmental Panel on Climate Change AR4 models using equidistant quantile matching, *J. Geophys. Res.-Atmos.*, 115, <https://doi.org/10.1029/2009JD012882>, 2010.

- Luo, M., Liu, T., Meng, F., Duan, Y., Frankl, A., Bao, A., and De Maeyer, P.: Comparing bias correction methods used in down-scaling precipitation and temperature from regional climate models: A case study from the Kaidu River basin in western China, *Water*, 10, 1046, <https://doi.org/10.3390/w10081046>, 2018.
- Lutz, A. F., Immerzeel, W. W., Kraaijenbrink, P. D., Shrestha, A. B., and Bierkens, M. F.: Climate change impacts on the upper Indus hydrology: sources, shifts and extremes, *PLoS One*, 11, e0165630, <https://doi.org/10.1371/journal.pone.0165630>, 2016.
- Marzeion, B., Hock, R., Anderson, B., Bliss, A., Champollion, N., Fujita, K., Huss, M., Immerzeel, W. W., Kraaijenbrink, P., Malles, J., Maussion, F., Radić, V., Rounce, D. R., Sakai, A., Shannon, S., Van De Wal, R., and Zekollari, H.: Partitioning the Uncertainty of Ensemble Projections of Global Glacier Mass Change, *Earth's Future*, 8, e2019EF001470, <https://doi.org/10.1029/2019EF001470>, 2020.
- Matthews, T., Perry, L. B., Koch, I., Aryal, D., Khadka, A., Shrestha, D., Abernathy, K., Elmore, A. C., Seimon, A., Tait, A., Elvin, S., Tuladhar, S., Baidya, S. K., Potocki, M., Birkel, S. D., Kang, S., Sherpa, T. C., Gajurel, A., and Mayewski, P. A.: Going to Extremes: Installing the World's Highest Weather Stations on Mount Everest, *B. Am. Meteorol. Soc.*, 101, E1870–E1890, <https://doi.org/10.1175/BAMS-D-19-0198.1>, 2020.
- Maurer, J. M., Schaefer, J. M., Rupper, S., and Corley, A.: Acceleration of ice loss across the Himalayas over the past 40 years, *Sci. Adv.*, 5, eaav7266, <https://doi.org/10.1126/sciadv.aav7266>, 2019.
- Miles, E. S., Willis, I., Buri, P., Steiner, J. F., Arnold, N. S., and Pellicciotti, F.: Surface Pond Energy Absorption Across Four Himalayan Glaciers Accounts for 1/8 of Total Catchment Ice Loss, *Geophys. Res. Lett.*, 45, <https://doi.org/10.1029/2018GL079678>, 2018a.
- Miles, K. E., Hubbard, B., Quincey, D. J., Miles, E. S., Sherpa, T. C., Rowan, A. V., and Doyle, S. H.: Polythermal structure of a Himalayan debris-covered glacier revealed by borehole thermometry, *Sci. Rep.*, 8, 16825, <https://doi.org/10.1038/s41598-018-34327-5>, 2018b.
- Miles, K. E., Hubbard, B., Miles, E. S., Quincey, D. J., Rowan, A. V., Kirkbride, M., and Hornsey, J.: Continuous borehole optical televiewing reveals variable englacial debris concentrations at Khumbu Glacier, Nepal, *Commun. Earth Environ.*, 2, 12, <https://doi.org/10.1038/s43247-020-00070-x>, 2021.
- Miles, K. E., Hubbard, B., Miles, E. S., Quincey, D. J., and Rowan, A. V.: Internal structure of a Himalayan debris-covered glacier revealed by borehole optical televiewing, *J. Glaciol.*, 69, 811–822, <https://doi.org/10.1017/jog.2022.100>, 2022.
- Mölg, T., Maussion, F., Yang, W., and Scherer, D.: The footprint of Asian monsoon dynamics in the mass and energy balance of a Tibetan glacier, *The Cryosphere*, 6, 1445–1461, <https://doi.org/10.5194/tc-6-1445-2012>, 2012.
- Mölg, T., Maussion, F., and Scherer, D.: Mid-latitude westerlies as a driver of glacier variability in monsoonal High Asia, *Nat. Clim. Change*, 4, 68–73, <https://doi.org/10.1038/nclimate2055>, 2014.
- Mott, R., Stiperski, I., and Nicholson, L.: Spatio-temporal flow variations driving heat exchange processes at a mountain glacier, *The Cryosphere*, 14, 4699–4718, <https://doi.org/10.5194/tc-14-4699-2020>, 2020.
- Nakawo, M.: Processes Which Distribute Supraglacial Debris On The Khumbu Glacier, Nepal Himalaya, *Ann. Glaciol.*, 8, <https://doi.org/10.3189/S0260305500001294>, 1986.
- Nicholson, L., Wirbel, A., Mayer, C., and Lambrecht, A.: The Challenge of Non-Stationary Feedbacks in Modeling the Response of Debris-Covered Glaciers to Climate Forcing, *Front. Earth Sci.*, 9, 662695, <https://doi.org/10.3389/feart.2021.662695>, 2021.
- Oerlemans, J.: *Glaciers and climate change*, CRC Press, eBook ISBN 9781003760672, 2001.
- Oulkar, S. N., Peacey, M. W., Mitrev, M., Quincey, D. J., Hubbard, B., Matthews, T., Oulkar, A. S., Miles, K. E., and Rowan, A. V.: Design and implementation of a robust data logging and satellite telemetry system for remote cryospheric research, *Geosci. Instrum. Method. Data Syst.*, 15, 75–88, <https://doi.org/10.5194/gi-15-75-2026>, 2026.
- Owen, L. A., Robinson, R., Benn, D. I., Finkel, R. C., Davis, N. K., Yi, C., Putkonen, J., Li, D., and Murray, A. S.: Quaternary glaciation of Mount Everest, *Quaternary Sci. Rev.*, 28, 1412–1433, <https://doi.org/10.1016/j.quascirev.2009.02.010>, 2009.
- Pedersen, J. S. T., Van Vuuren, D. P., Aparício, B. A., Swart, R., Gupta, J., and Santos, F. D.: Variability in historical emissions trends suggests a need for a wide range of global scenarios and regional analyses, *Commun. Earth Environ.*, 1, 41, <https://doi.org/10.1038/s43247-020-00045-y>, 2020.
- Pellicciotti, F., Stephan, C., Miles, E., Herreid, S., Immerzeel, W. W., and Bolch, T.: Mass-balance changes of the debris-covered glaciers in the Langtang Himal, Nepal, from 1974 to 1999, *J. Glaciol.*, 61, 373–386, <https://doi.org/10.3189/2015JoG13J237>, 2015.
- Pepin, N. C., Arnone, E., Gobiet, A., Haslinger, K., Kotlarski, S., Notarnicola, C., Palazzi, E., Seibert, P., Serafin, S., Schöner, W., Terzago, S., Thornton, J. M., Vuille, M., and Adler, C.: Climate Changes and Their Elevational Patterns in the Mountains of the World, *Rev. Geophys.*, 60, <https://doi.org/10.1029/2020RG000730>, 2022.
- Piani, C., Weedon, G. P., Best, M., Gomes, S. M., Viterbo, P., Hagemann, S., and Haerter, J. O.: Statistical bias correction of global simulated daily precipitation and temperature for the application of hydrological models, *J. Hydrol.*, 395, 199–215, <https://doi.org/10.1016/j.jhydrol.2010.10.024>, 2010.
- Pierce, D. W., Barnett, T. P., Santer, B. D., and Gleckler, P. J.: Selecting global climate models for regional climate change studies, *P. Natl. Acad. Sci. USA*, 106, 8441–8446, <https://doi.org/10.1073/pnas.0900094106>, 2009.
- Potocki, M., Mayewski, P. A., Matthews, T., Perry, L. B., Schwikowski, M., Tait, A. M., Korotkikh, E., Clifford, H., Kang, S., Sherpa, T. C., Singh, P. K., Koch, I., and Birkel, S.: Mt. Everest's highest glacier is a sentinel for accelerating ice loss, *npj Clim. Atmos. Sci.*, 5, 7, <https://doi.org/10.1038/s41612-022-00230-0>, 2022.
- Pritchard, H. D.: Asia's shrinking glaciers protect large populations from drought stress, *Nature*, 569, 649–654, <https://doi.org/10.1038/s41586-019-1240-1>, 2019.
- Purdie, H., Kerr, T., Robson, B., Anderson, B., Lorrey, A. M., Rack, W., Brasington, J., and Bealing, P.: Mass balance characteristics of the “vanishing” Rolleston Glacier, New Zealand, *Ann. Glaciol.*, 66, e31, <https://doi.org/10.1017/aog.2025.10032>, 2025.
- Quincey, D. J., Luckman, A., and Benn, D.: Quantification of Everest region glacier velocities between 1992 and 2002, using satel-

- lite radar interferometry and feature tracking, *J. Glaciol.*, 55, 596–606, <https://doi.org/10.3189/002214309789470987>, 2009.
- Ragetli, S., Immerzeel, W. W., and Pellicciotti, F.: Contrasting climate change impact on river flows from high-altitude catchments in the Himalayan and Andes Mountains, *P. Natl. Acad. Sci. USA*, 113, 9222–9227, <https://doi.org/10.1073/pnas.1606526113>, 2016.
- Reiter, P., Gutjahr, O., Schefczyk, L., Heinemann, G., and Casper, M.: Does applying quantile mapping to subsamples improve the bias correction of daily precipitation?, *Int. J. Climatol.*, 38, 1623–1633, 2018.
- RGI 7.0 Consortium: A Dataset of Global Glacier Outlines, Version 7.0. Boulder, Colorado USA. NSIDC: National Snow and Ice Data Center [data set], <https://doi.org/10.5067/f6jmovy5navz>, 2023.
- Roering, J. J., Kirchner, J. W., and Dietrich, W. E.: Evidence for nonlinear, diffusive sediment transport on hillslopes and implications for landscape morphology, *Water Resour. Res.*, 35, 853–870, <https://doi.org/10.1029/1998WR900090>, 1999.
- Rounce, D. R., Hock, R., Maussion, F., Hugonnet, R., Kochtitzky, W., Huss, M., Berthier, E., Brinkerhoff, D., Compagno, L., Copland, L., Farinotti, D., Menounos, B., and McNabb, R. W.: Global glacier change in the 21st century: Every increase in temperature matters, *Science*, 379, 78–83, <https://doi.org/10.1126/science.abo1324>, 2023.
- Rowan, A. V.: The “Little Ice Age” in the Himalaya: A review of glacier advance driven by Northern Hemisphere temperature change, *The Holocene*, 27, 292–308, <https://doi.org/10.1177/0959683616658530>, 2017.
- Rowan, A. and Pedersen, V. K.: annrowan/isosia: iSOSIA version used in Schlich-Davies et al. (spm-3.3.3r), Zenodo [code], <https://doi.org/10.5281/zenodo.12666864>, 2024.
- Rowan, A. V., Egholm, D. L., Quincey, D. J., and Glasser, N. F.: Modelling the feedbacks between mass balance, ice flow and debris transport to predict the response to climate change of debris-covered glaciers in the Himalaya, *Earth Planet. Sc. Lett.*, 430, 427–438, <https://doi.org/10.1016/j.epsl.2015.09.004>, 2015.
- Rowan, A. V., Egholm, D. L., Quincey, D. J., Hubbard, B., King, O., Miles, E. S., Miles, K. E., and Hornsey, J.: The Role of Differential Ablation and Dynamic Detachment in Driving Accelerating Mass Loss From a Debris-Covered Himalayan Glacier, *J. Geophys. Res.-Earth*, 126, <https://doi.org/10.1029/2020JF005761>, 2021.
- Ruane, A. C., Goldberg, R., and Chryssanthacopoulos, J.: Climate forcing datasets for agricultural modeling: Merged products for gap-filling and historical climate series estimation, *Agr. Forest Meteorol.*, 200, 233–248, <https://doi.org/10.1016/j.agrformet.2014.09.016>, 2015.
- Salerno, F., Guyennon, N., Thakuri, S., Viviano, G., Romano, E., Vuillermoz, E., Cristofanelli, P., Stocchi, P., Agrillo, G., Ma, Y., and Tartari, G.: Weak precipitation, warm winters and springs impact glaciers of south slopes of Mt. Everest (central Himalaya) in the last 2 decades (1994–2013), *The Cryosphere*, 9, 1229–1247, <https://doi.org/10.5194/tc-9-1229-2015>, 2015.
- Salerno, F., Guyennon, N., Yang, K., Shaw, T. E., Lin, C., Colombo, N., Romano, E., Gruber, S., Bolch, T., Alessandri, A., Cristofanelli, P., Putero, D., Diolaiuti, G., Tartari, G., Verza, G., Thakuri, S., Balsamo, G., Miles, E. S., and Pellicciotti, F.: Local cooling and drying induced by Himalayan glaciers under global warming, *Nat. Geosci.*, 16, 1120–1127, <https://doi.org/10.1038/s41561-023-01331-y>, 2023.
- Sanjay, J., Krishnan, R., Shrestha, A. B., Rajbhandari, R., and Ren, G.-Y.: Downscaled climate change projections for the Hindu Kush Himalayan region using CORDEX South Asia regional climate models, *Advances in Climate Change Research*, 8, 185–198, <https://doi.org/10.1016/j.accre.2017.08.003>, 2017.
- Sauter, T., Arndt, A., and Schneider, C.: COSIPY v1.3 – an open-source coupled snowpack and ice surface energy and mass balance model, *Geosci. Model Dev.*, 13, 5645–5662, <https://doi.org/10.5194/gmd-13-5645-2020>, 2020.
- Shaw, T. E., Miles, E. S., Chen, D., Jouberton, A., Kneib, M., Fugger, S., Ou, T., Lai, H.-W., Fujita, K., Yang, W., Fatichi, S., and Pellicciotti, F.: Multi-decadal monsoon characteristics and glacier response in High Mountain Asia, *Environ. Res. Lett.*, 17, 104001, <https://doi.org/10.1088/1748-9326/ac9008>, 2022.
- Shaw, T. E., Buri, P., McCarthy, M., Miles, E. S., and Pellicciotti, F.: Local Controls on Near-Surface Glacier Cooling Under Warm Atmospheric Conditions, *J. Geophys. Res.-Atmos.*, 129, e2023JD040214, <https://doi.org/10.1029/2023JD040214>, 2024.
- Shaw, T. E., Miles, E. S., McCarthy, M., Buri, P., Guyennon, N., Salerno, F., Carturan, L., Brock, B., and Pellicciotti, F.: Mountain glaciers recouple to atmospheric warming over the twenty-first century, *Nat. Clim. Change*, 15, 1212–1218, <https://doi.org/10.1038/s41558-025-02449-0>, 2025.
- Shea, J. M., Immerzeel, W. W., Wagnon, P., Vincent, C., and Bajracharya, S.: Modelling glacier change in the Everest region, Nepal Himalaya, *The Cryosphere*, 9, 1105–1128, <https://doi.org/10.5194/tc-9-1105-2015>, 2015.
- Sherpa, S. F., Wagnon, P., Brun, F., Berthier, E., Vincent, C., Lejeune, Y., Arnaud, Y., Kayastha, R. B., and Sinisalo, A.: Contrasted surface mass balances of debris-free glaciers observed between the southern and the inner parts of the Everest region (2007–15), *J. Glaciol.*, 63, 637–651, <https://doi.org/10.1017/jog.2017.30>, 2017.
- Strickland, R. M., Covington, M. D., Gulley, J. D., Kayastha, R. B., and Blackstock, J. M.: Englacial Drainage Drives Positive Feedback Depression Growth on the Debris-Covered Ngozumpa Glacier, Nepal, *Geophys. Res. Lett.*, 50, e2023GL104389, <https://doi.org/10.1029/2023GL104389>, 2023.
- Sun, W., Qin, X., Wang, Y., Chen, J., Wentao, D., Tong, Z., and Huai, B.: The response of surface mass and energy balance of a continental glacier to climate variability, western Qilian Mountains, China, *Clim. Dynam.*, 50, 3557–3570, <https://doi.org/10.1007/s00382-017-3823-6>, 2018.
- Ueno, K., Toyotsu, K., Bertolani, L., and Tartari, G.: Stepwise Onset of Monsoon Weather Observed in the Nepal Himalaya, *Mon. Weather Rev.*, 136, 2507–2522, <https://doi.org/10.1175/2007MWR2298.1>, 2008.
- Vacco, D. A., Alley, R. B., and Pollard, D.: Glacial advance and stagnation caused by rock avalanches, *Earth Planet. Sc. Lett.*, 294, 123–130, <https://doi.org/10.1016/j.epsl.2010.03.019>, 2010.
- Vrac, M., Stein, M. L., Hayhoe, K., and Liang, X. Z.: A general method for validating statistical downscaling methods under future climate change, *Geophys. Res. Lett.*, 34, <https://doi.org/10.1029/2007GL030295>, 2007.
- Wagnon, P., Lafaysse, M., Lejeune, Y., Maisincho, L., Rojas, M., and Chazarin, J. P.: Understanding and modeling the physical processes that govern the melting of snow cover in a tropi-

- cal mountain environment in Ecuador, *J. Geophys. Res.-Atmos.*, 114, <https://doi.org/10.1029/2009JD012292>, 2009.
- Watson, C. S., Quincey, D. J., Smith, M. W., Carrivick, J. L., Rowan, A. V., and James, M. R.: Quantifying ice cliff evolution with multi-temporal point clouds on the debris-covered Khumbu Glacier, Nepal, *J. Glaciol.*, 63, 823–837, <https://doi.org/10.1017/jog.2017.47>, 2017.
- Wirbel, A., Jarosch, A. H., and Nicholson, L.: Modelling debris transport within glaciers by advection in a full-Stokes ice flow model, *The Cryosphere*, 12, 189–204, <https://doi.org/10.5194/tc-12-189-2018>, 2018.
- Wohlfahrt, G., Hammerle, A., Haslwanter, A., Bahn, M., Tappeiner, U., and Cernusca, A.: Disentangling leaf area and environmental effects on the response of the Net Ecosystem CO₂ Exchange to diffuse radiation, *Geophys. Res. Lett.*, 35, <https://doi.org/10.1029/2008gl035090>, 2008.
- Wohlfahrt, G., Hammerle, A., Niedrist, G., Scholz, K., Tomelleri, E., and Zhao, P.: On the energy balance closure and net radiation in complex terrain, *Agr. Forest Meteorol.*, 226–227, 37–49, <https://doi.org/10.1016/j.agrformet.2016.05.012>, 2016.
- Yang, K., Guyennon, N., Ouyang, L., Tian, L., Tartari, G., and Salerno, F.: Impact of summer monsoon on the elevation-dependence of meteorological variables in the south of Central Himalaya, *Int. J. Climatol.*, 38, 1748–1759, <https://doi.org/10.1002/joc.5293>, 2017.